Inorganic Chemistry

pubs.acs.org/IC

Article

Synthesis, Characterization, and Cytotoxicity of Morpholine-Containing Ruthenium(II) *p*-Cymene Complexes

Rishav Chatterjee,[†] Indira Bhattacharya,[†] Souryadip Roy, Kallol Purkait, Tuhin Subhra Koley, Arnab Gupta,* and Arindam Mukherjee*

Cite This: https://doi.org/10.1021/acs.inorgchem.1c01363

Read Online

ACCESS | Metrics & More | Article Recommendations | Supporting Information

ABSTRACT: Morpholine motif is an important pharmacophore and, depending on the molecular design, may localize in cellular acidic vesicles. To understand the importance of the presence of pendant morpholine in a metal complex, six bidentate N,O-donor ligands with or without a pendant morpholine unit and their corresponding ruthenium(II) *p*-cymene complexes (**1**−**6**) are synthesized, purified, and structurally characterized by various analytical methods including X-ray diffraction. Complexes **2**−**4** crystallized in the $P2_1/c$ space group, whereas **5** and **6** crystallized in the $P\bar{1}$ space group. The solution stability studies using ^{1}H NMR support instantaneous hydrolysis of the native complexes to form monoaquated species in a solution of 3:7 (v/v) dimethyl sulfoxide-d_6 and 20 mM phosphate buffer (pH* 7.4, containing 4 mM NaCl). The monoaquated complexes are stable for at least up to 24 h. The complexes display excellent in vitro antiproliferative activity (IC_{50} ca. 1−14 μM) in various cancer cell lines, viz., MDA-MB-231, MiaPaCa2, and Hep-G2. The presence of the pendant morpholine does not improve the dose efficacy, but rather, with 2-[[(2,6-dimethylphenyl)imino]methyl]phenol (HL1) and its pendant morpholine analogue (HL3) giving complexes **1** and **3**, respectively, the antiproliferative activity was poorer with **3**. MDA-MB-231 cells treated with the complexes show that the acidic vesicles remain acidic, but the population of acidic vesicles increases or decreases with time of exposure, as observed from the dispersed red puncta, depending on the complex used. The presence of the 2,6-disubstituted aniline and the naphthyl group seems to improve the antiproliferative dose. The complex treated MDA-MB-231 cells show that cathepsin D, which is otherwise present in the cytosolic lysosomes, translocates to the nucleus as a result of exposure to the complexes. Irrespective of the presence of a morpholine motif, the complexes do not activate caspase-3 to induce apoptosis and seem to favor the necrotic pathway of cell killing.

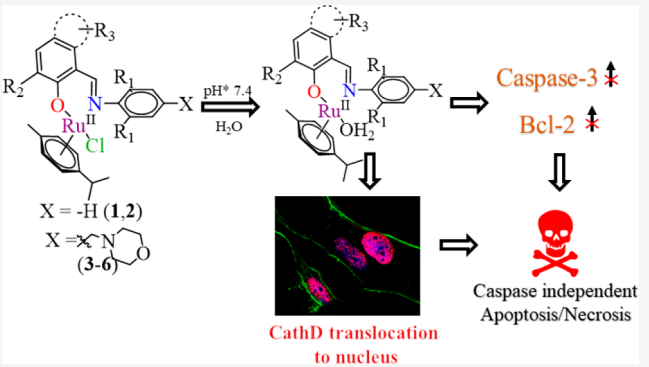

INTRODUCTION

Platinum drugs have displayed high cure rates for testicular cancer and are used to treat various other tumors, viz., prostate, colon, ovarian, esophageal, bladder, head and neck, and nonsmall cell lung cancer.[1−4] Platinum drugs are also known for their poor tumor selectivity, serious side effects, and intrinsic and/or acquired resistance, making them ineffective for treatment against several tissue types.[2,5,6] Thus, in spite of its clinical success, the deleterious side effects of cisplatin have led to the search for new anticancer agents with improved therapeutics. The goal of the modern design by changing the metal and tuning ligand properties encompasses the reduction of adverse side effects, activation by external stimuli, and a focus on targets other than the nucleus to avoid mutagenic character and improve delivery.[7−14] Metal complexes with potential apart from platinum(II/IV) include gallium(II) and ruthenium(II/III).[15−21] Gallium(III) nitrate has been effective against lymphoma and bladder cancer.[22] Gallium(III) maltolate and tris(8-quinolinolato)gallium(III) have shown efficiency against hepatocellular carcinoma and renal carcinoma, respectively.[15,16,22]

Ruthenium(II/III) complexes have raised considerable interest because of the shelf-stability of the complexes in two oxidation states, the variation of kinetic inertness based on the oxidation states and geometry, and the scope of the incorporation of targeting motifs in the ligand without sacrificing the activity.[23−37] Ruthenium(III) complexes act as prodrugs because of the inert nature of the ruthenium(III) oxidation state. In a *lower oxygen environment* (hypoxia) of tumor cells, ruthenium(III) complexes get reduced to the more reactive ruthenium(II) complexes, providing enhanced toxicity

Received: May 7, 2021

in tumors.[38] The high binding affinity of ruthenium(III) for the transferrin iron-binding sites offers the possibility of targeting tumors with high transferrin receptor densities.[39−41] Two ruthenium(II/III) complexes, KP1339 and TLD-1433, are currently undergoing clinical trials as anticancer agents. KP1339 is a ruthenium(III) complex that has undergone clinical trials against various solid tumors, including nonsmall cell lung carcinoma and neuroendocrine tumors.[20] TLD-1433 is the first ruthenium complex that has entered clinical trials, as a photodynamic therapy agent against BCG refractory/intolerant nonmuscle invasive bladder cancer.[17,18] Controlled multistep synthesis helps to incorporate various ligands of interest to render optimized ruthenium complexes with efficient antitumor activity.[7,25,31,42−48]

In the past few decades, ruthenium(II) half-sandwich complexes with piano-stool configurations provided researchers the opportunity to design various organic ligands involving certain targets and then coordinate them to ruthenium(II) arenes and monitor their activity, selectivity, and kinetic properties.[49−62] Among the various motifs used as pharmacophores, morpholine is found in various anticancer drugs (Figure 1). The incorporation of morpholine may enhance the

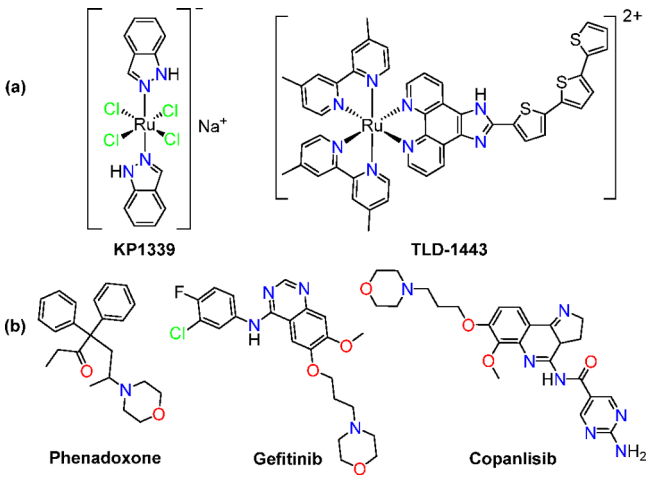

Figure 1. (a) Anticancer ruthenium complexes in clinical trials. (b) Clinical drugs containing a morpholine moiety.

activity, selectivity, solubility, bioavailability, and pharmacokinetic benefits.[63−65] Compounds with morpholine motifs target various enzymes and receptors including kinases, Amyloid β peptides, α-glucosidase, serotonin receptors, and histamine receptors.[66−74] Morpholine is also known to help target lysosomes in cells and acts as the cells' recycling apparatus.[75,76] The work presented here compares the presence and absence of the morpholine motif in N,O-donor bidentate ligands in a metal complex, keeping the rest of the environment the same. Six new ruthenium(II) *p*-cymene complexes with N,O-donor Schiff bases with or without pendant morpholine motifs were synthesized and characterized for this purpose.

EXPERIMENTAL SECTION

Materials and Methods. The chemicals and solvents were purchased from various commercial sources. Unless specifically mentioned, the chemicals were used as received without further purification. Solvents were dried following standard procedures.[77] 3-(4,5-Dimethylthiazol-2-yl)-2,5-diphenyltetrazolium bromide (MTT) and the biological assay kits were purchased from Gibco. Solvents used for spectroscopic measurements were of spectroscopic grade and purchased from Spectrochem, India. A PerkinElmer Lambda 35 spectrophotometer was used for UV−vis measurements. The Fourier transform infrared (FT-IR) spectra were recorded using a PerkinElmer SPECTRUM RX I spectrometer in KBr pellets. ^{1}H NMR, ^{13}C NMR, and HMQC spectra were recorded using either a 400 MHz JEOL ECS or 500 MHz Bruker Avance III spectrometer at room temperature (24−27 °C). All of the ^{13}C NMR spectra reported are proton-decoupled. The chemical shifts of the relevant compounds are reported in parts per million (ppm). All of the mass spectrometry (ESI-MS) spectra were recorded in positive-mode electrospray ionization using a Bruker maXis II instrument. The reported yields are of ^{1}H NMR pure compounds.

Synthesis and Characterization. *Syntheses of Schiff Base Ligands. General Procedure I.* A literature procedure was adapted for synthesis of the amine (**B2** or **B3**).[78,79] To a methanolic solution of the desired aniline (**B1**/**B2**/**B3**; 1 mmol) was added the corresponding aldehyde (1 mmol), and the solution was heated to reflux for 24 h. After the mixture was cooled, the desired compound precipitated. The precipitate was filtered, washed with cold methanol (MeOH) and hexane, and dried under vacuum.

General Procedure II. A literature procedure was adapted for synthesis of the amine **B2**.[78] To a stirred solution of the respective aniline (**B1**/**B2**; 1 mmol) in MeOH was added the corresponding aldehyde (1 mmol), and the resulting solution was refluxed for 24 h. After the mixture was cooled, the solvent was evaporated in a rotary evaporator, which resulted in a yellow oil. The oil used was further purified by silica gel column chromatography [mobile phase: 3:2 (v/v) hexane/ ethyl acetate].

*Synthesis of (E)-2-[[(2,6-Dimethylphenyl)imino]methyl]phenol (**HL1**).* **HL1** was synthesized by general procedure II and used without purification. Yield: 91%, yellow oil. ^{1}H NMR (400 MHz, $CDCl_3$): δ 8.35 (s, 1H, CH═N), 7.45−7.39 (m, 1H, Ar−H), 7.35 (dd, J = 7.6 and 1.6 Hz, 1H, Ar−H), 7.12 (d, J = 7.5 Hz, 2H, Ar−H), 7.09−7.03 (m, 2H), 6.98 (dd, 1H, J = 7.4 and 1.0 Hz, Ar−H), 2.22 (s, 6H) (Figure S1). ^{13}C NMR (100 MHz, $CDCl_3$): δ 166.8, 161.3, 148.2, 133.3, 132.3, 128.6, 128.4, 125.0, 119.1, 118.9, 117.4, 18.6 (Figure S2).

*Synthesis of (E)-1-[[(2,6-Dimethylphenyl)imino]methyl]-naphthalen-2-ol (**HL2**).* **HL2** was synthesized by general procedure I. Yield: 62%, yellow solid. ^{1}H NMR (500 MHz, $CDCl_3$): δ 9.12 (s, 1H, CH═N), 7.99 (d, J = 8.5 Hz, 1H, Ar−H), 7.86 (d, J = 9.1 Hz, 1H, Ar−H), 7.76 (d, J = 8.0 Hz, 1H, Ar−H), 7.51 (t, J = 7.6 Hz, 1H, Ar−H), 7.35 (t, J = 7.4 Hz, 1H, Ar−H), 7.23 (d, J = 9.1 Hz, 1H, Ar−H), 7.17 (d, J = 7.4 Hz, 2H, Ar−H), 7.13−7.08 (m, 1H, Ar−H), 2.32 (s, 6H, Ar−CH_3) (Figure S3). ^{13}C NMR (125 MHz, $CDCl_3$): δ 168, 161.3, 145.5, 136.2, 133.2, 129.7, 129.3, 128.6, 128.1, 127.4, 125.8, 123.5, 121.4, 118.8, 108.3, 18.6 (Figure S4).

*Synthesis of 2-[[[2,6-Dimethyl-4-(morpholinomethyl)phenyl]-imino]methyl]phenol (**HL3**).* **HL3** was synthesized by general procedure I. Yield: 79%, light-yellow solid. ^{1}H NMR (500 MHz, $CDCl_3$): δ 13.08 (s, 1H, OH), 8.34 (s, 1H), 7.40 (t, J = 7.2 Hz, 1H, CH═N), 7.34 (d, J = 7.6 Hz, 1H, Ar−H), 7.05 (d, J = 11.2 Hz, 3H, Ar−H), 6.95 (t, J = 7.4 Hz, 1H, Ar−H), 3.74 (d, J = 4.0 Hz, 4H, −O−CH_2), 3.45 (s, 2H, Ar−CH_2), 2.48 (s, 4H, N−CH_2), 2.19 (s, 6H, Ar−CH_3) (Figure S5). ^{13}C NMR (125 MHz, $CDCl_3$): δ 166.7, 161.2, 147.2, 134.2, 133.2, 132.1, 129.2, 128.2, 119.0, 118.8, 117.3, 67.0, 63.1, 53.7, 18.5 (Figure S6).

*Synthesis of 2-[[[2,6-Dimethyl-4-(morpholinomethyl)phenyl]-imino]methyl]-6-methoxyphenol (**HL4**).* **HL4** was synthesized by general procedure II. Yield: 53%, yellow oil. ^{1}H NMR (500 MHz, $CDCl_3$): δ 13.52 (s, 1H, O−H), 8.34 (s, 1H, CH═N), 7.06 (s, 2H, Ar−H), 7.01 (d, J = 7.8 Hz, 1H, Ar−H), 6.96 (d, J = 7.6 Hz, 1H, Ar−H), 6.90 (t, J = 7.7 Hz, 1H, Ar−H), 3.95 (s, 3H, O−CH_3), 3.73 (s, 4H, O−CH_2), 3.44 (s, 2H, Ar−CH_2), 2.47 (s, 4H, N−CH_2), 2.19 (s, 6H, Ar−CH_3) (Figure S7). ^{13}C NMR (125 MHz, $CDCl_3$): δ 166.8, 151.4, 148.5, 146.9, 134.1, 129.2, 128.3, 123.5, 118.6, 118.5, 114.6, 66.9, 63, 56.1, 53.6, 18.5 (Figure S8).

*Synthesis of 1-[[[2,6-Dimethyl-4-(morpholinomethyl)phenyl]-imino]methyl]naphthalen-2-ol (**HL5**).* **HL5** was synthesized by general procedure II. Yield: 49%, yellow crystalline solid. ^{1}H NMR

https://doi.org/10.1021/acs.inorgchem.1c01363
Inorg. Chem. XXXX, XXX, XXX−XXX

(400 MHz, $CDCl_3$): δ 9.10 (s, 1H, CH═N), 7.97 (d, J = 8.4 Hz, 1H, Ar−H), 7.83 (d, J = 9.2 Hz, 1H, Ar−H), 7.74 (d, J = 8.0 Hz, 1H, Ar−H), 7.48 (dt, J = 8.3, 6.8, and 1.2 Hz, 1H, Ar−H), 7.36−7.31 (m, 1H, Ar−H), 7.16 (d, J = 9.1 Hz, 1H, Ar−H), 7.12 (s, 2H, Ar−H), 3.77−3.73 (m, 4H, O−CH_2), 3.48 (s, 2H, −CH_2), 2.52−2.47 (m, 4H, N−CH_2), 2.30 (s, 6H, Ar−CH_3) (Figure S9). ^{13}C NMR (100 MHz, $CDCl_3$): δ 168.3, 161.2, 144.3, 136.1, 134.1, 133.2 129.7, 129.6, 129.4, 128.1, 127.4, 123.5, 121.7, 118.8, 108.4, 67.0, 63.1, 53.7, 18.8 (Figure S10).

*Synthesis of (E)-1-[[[2,6-Diisopropyl-4-(morpholinomethyl)-phenyl]imino]methyl]naphthalen-2-ol (**HL6**).* **HL6** was synthesized by general procedure I. Yield: 58%, yellow solid. ^{1}H NMR (500 MHz, $CDCl_3$): δ 15.22 (s, 1H, O−H), 9.07 (d, J = 2.5 Hz, 1H, CH═N), 7.99 (d, J = 8.5 Hz, 1H, Ar−H), 7.86 (d, J = 9.1 Hz, 1H, Ar−H), 7.77 (d, J = 8.0 Hz, 1H, Ar−H), 7.49 (t, J = 7.7 Hz, 1H, Ar−H), 7.35 (t, J = 7.5 Hz, 1H, Ar−H), 7.19 (d, J = 7.6 Hz, 3H, Ar−H), 3.76 (d, J = 3.8 Hz, 4H, O−CH_2), 3.56 (s, 2H, Ar−CH_2), 3.11 (m, 2H, ^{i}Pr−CH), 2.51 (s, 4H, N−CH_2), 1.24 (d, J = 6.8 Hz, 12H, ^{i}Pr−CH_3) (Figure S11). ^{13}C NMR (125 MHz, $CDCl_3$): δ 167.7, 161.6, 142.8, 140.2, 135.9, 135.3, 133.2, 129.3, 128.1, 127.4, 124.3, 123.4, 121.5, 118.7, 108.3, 67, 63.4, 53.5, 28.3, 23.7 (Figure S12).

Syntheses of Metal Complexes. *General Procedure for the Synthesis of Metal Complexes **1**−**6**.* To a 10 mL stirred methanolic solution of 0.2 mmol of the respective ligand was added 0.2 mmol of solid KOH. After 15 min, a 10 mL methanolic solution of 0.1 mmol of $Ru_2(p\text{-cym})_2Cl_4$ was added (in the dark), and the resultant solution was left under stirring for 12 h at 25 °C. The entire solution was evaporated to dryness, washed multiple times with a minimal amount of diethyl ether, and purified by column chromatography using neutral alumina. The mobile phase was 19:1 (v/v) dichloromethane/MeOH.

*Ru(p-cym)(**L1**)Cl (**1**).* Yield: 71%. ^{1}H NMR (400 MHz, DMSO-d_6): δ 7.59 (s, 1H, CH═N), 7.24 (m, 2H, Ar−H), 7.21 (m, 1H, Ar−H), 7.09 (t, J = 6.9 Hz, 1H, Ar−H), 7.01 (d, J = 6.4 Hz, 1H, Ar−H), 6.64 (d, J = 8.4 Hz, 1H, Ar−H), 6.31 (t, J = 7.2 Hz, 1H, Ar−H), 5.32 (d, J = 6.0 Hz, 1H, p-cym−H), 5.14 (d, J = 6.1 Hz, 1H, p-cym−H), 5.06 (d, J = 5.7 Hz, 1H, p-cym−H), 4.26 (d, J = 5.6 Hz, 1H, p-cym−H), 2.54 (m, 1H, p-cym−^{i}Pr), 2.45 (s, 3H, Ar−CH_3), 2.19 (s, 3H, Ar−CH_3), 1.89 (s, 3H, Ar−CH_3), 1.21 (d, J = 6.9 Hz, 6H, p-cym−^{i}Pr) (Figure S13). ^{13}C NMR (125 MHz, DMSO-d_6): δ 166.6, 165.9, 154.6, 135.3, 134.5, 131.1, 130.5, 128.6, 128, 126.3, 121, 120.5, 113.1, 102.9, 94.2, 85.8, 84.4, 82.1, 79.1, 30.3, 22, 21.8, 19.2, 18.1, 17 (Figure S14). IR (KBr pellets, cm^{-1}): 1584 (CH═N) (Figure S29). UV−vis [MeOH; λ_{max}, nm (ε, M^{-1} cm^{-1})]: 241 (18620), 292 (5950), 405 (1600), 483 (840) (Figure S28). ESI-HRMS (MeOH). m/z (exp) 460.1214 (460.1281) [$Ru^{II}C_{25}H_{28}NO^+$]. Anal. Calcd for $C_{25}H_{28}ClNORu$: C, 60.66; H, 5.70; N, 2.83. Found: C, 60.84; H, 5.75; N, 2.79.

*Ru(p-cym)(**L2**)Cl (**2**).* Yield: 78%. ^{1}H NMR (500 MHz, DMSO-d_6): δ 7.99 (s, 1H, CH═N), 7.66−7.59 (m, 3H, Ar−H), 7.25 (m, 4H, Ar−H), 7.12 (t, J = 7.3 Hz, 1H, Ar−H), 6.95 (d, J = 9.2 Hz, 1H, Ar−H), 5.34 (d, J = 6.1 Hz, 1H, p-cym−H), 5.19 (d, J = 6.0 Hz, 1H, p-cym−H), 5.07 (d, J = 5.7 Hz, 1H, p-cym−H), 4.33 (d, J = 5.8 Hz, 1H, p-cym−H), 2.63−2.59 (m, 1H, p-cym−^{i}Pr), 2.17 (s, 3H, Ar−CH_3), 1.93 (s, 3H, Ar−CH_3), 1.25 (dd, ^{J} = 10.4 and 7.0 Hz, 6H, p-cym−^{i}Pr). ^{13}C NMR (125 MHz, DMSO-d_6): δ 166.8, 158.4, 155.3, 134.8, 134.4, 131.5, 130.7, 128.5, 128.0, 127.3, 126.1, 125.6, 124.4, 121.6, 119.5, 111.2, 103.1, 94.0, 86.7, 84.7, 82.0, 79.4, 30.3, 22.0, 21.9, 19.1, 17.9, 17.0 (Figures S15−S17). IR (KBr pellets, cm^{-1}): 1582 (CH═N) (Figure S29). UV−vis [MeOH; λ_{max}, nm (ε, M^{-1} cm^{-1})]: 254 (34930), 321 (13120), 433 (3370), 485 (1670) (Figure S28). ESI-HRMS (MeOH). m/z (exp) 510.1371 (510.1345) [$Ru^{II}C_{29}H_{30}NO^+$]. Anal. Calcd for $C_{29}H_{30}ClNORu$: C, 63.90; H, 5.55; N, 2.57. Found: C, 63.77; H, 5.59; N, 2.62.

*Ru(p-cym)(**L3**)Cl (**3**).* Yield: 59%. ^{1}H NMR (500 MHz, DMSO-d_6): δ 7.58 (s, 1H, CH═N), 7.20 (s, 2H, Ar−H), 7.09 (t, J = 6.9 Hz, 1H, Ar−H), 7.01 (d, J = 7.2 Hz, 1H, Ar−H), 6.65 (d, J = 8.4 Hz, 1H, Ar−H), 6.31 (t, J = 6.9 Hz, 1H, Ar−H), 5.31 (d, J = 5.2 Hz, 1H, p-cym−H), 5.11 (d, J = 5.3 Hz, 2H, p-cym−H), 4.35 (d, J = 4.1 Hz, 1H, p-cym−H), 3.63 (s, 4H, O−CH_2), 3.50 (s, 2H, CH_2), 2.44 (s, 8H), 2.19 (s, 3H, CH_3), 1.90 (s, 3H, CH_3), 1.18 (dd, J = 16.8 and 6.7 Hz, 6H, p-cym−^{i}Pr). ^{13}C NMR (125 MHz, DMSO-d_6): δ 16.9, 18.0, 19.1, 21.5, 22.2, 30.1, 53.0, 66.1, 79.7, 82.8, 83.7, 84.8, 95.1, 102.3, 113.0, 120.4, 121.0, 128.8, 129.3, 130.3, 130.9, 134.5, 135.2, 165.8, 166.6 (Figures S18−S20). IR (KBr pellets, cm^{-1}): 1609 (CH═N) (Figure S29). UV−vis [MeOH; λ_{max}, nm (ε, M^{-1} cm^{-1})]: 244 (29550), 291 (8130), 403 (2300), 482 (1020) (Figure S28). ESI-HRMS (MeOH). m/z (exp) 559.1899 (559.1907) [$Ru^{II}C_{30}H_{37}N_2O_2^+$]. Anal. Calcd for $C_{30}H_{37}ClN_2O_2Ru$: C, 60.65; H, 6.28; N, 4.71. Found: C, 60.42; H, 6.33; N, 4.68.

*Ru(p-cym)(**L4**)Cl (**4**).* Yield: 54%. ^{1}H NMR (400 MHz, DMSO-d_6): δ 7.54 (s, 1H, CH═N), 7.17 (s, 2H, Ar−H), 6.70 (d, J = 7.3 Hz, 1H, Ar−H), 6.64 (d, J = 7.7 Hz, 1H, Ar−H), 6.23 (t, J = 7.6 Hz, 1H, Ar−H), 5.32 (d, J = 5.7 Hz, 1H, p-cym−H), 5.17 (d, J = 5.5 Hz, 1H, p-cym−H), 5.01 (d, J = 5.7 Hz, 1H, p-cym−H), 4.43 (d, J = 5.4 Hz, 1H, p-cym−H), 3.72 (s, 3H, O−CH_3), 3.62−3.59 (m, 4H, O−CH_2), 3.48 (s, 2H, CH_2), 2.41 (d, J = 10.2 Hz, 8H), 2.17 (s, 3H, Ar−CH_3), 1.90 (s, 3H, Ar−CH_3), 1.20−1.14 (m, 6H, p-cym−^{i}Pr) (Figure S21). ^{13}C NMR (100 MHz, DMSO-d_6): δ 165.6, 158.2, 153.5, 151.3, 135.4, 130.9, 130.3, 129.1, 128.5, 127.0, 120.3, 115.8, 112.1, 102.5, 95.5, 84.4, 83.7, 82.7, 79.9, 66.2, 61.9, 56.0, 29.9, 22.3, 21.5, 19.2, 18.1, 16.8 (Figure S22). IR (KBr pellets, cm^{-1}): 1601 (CH═N) (Figure S29). UV−vis [MeOH; λ_{max}, nm (ε, M^{-1} cm^{-1})]: 243 (28900), 304 (8630), 422 (1960), 490 (980) (Figure S28). ESI-HRMS (MeOH). m/z (exp) 589.2004 (589.1985) [$Ru^{II}C_{31}H_{39}N_2O_3^+$]. Anal. Calcd for $C_{31}H_{39}ClN_2O_3Ru$: C, 59.65; H, 6.30; N, 4.49. Found: C, 59.46; H, 6.27; N, 4.45.

*Ru(p-cym)(**L5**)Cl (**5**).* Yield: 62%. ^{1}H NMR (400 MHz, DMSO-d_6): δ 7.98 (s, 1H, CH═N), 7.62 (m, 3H, Ar−H), 7.26 (t, J = 7.5 Hz, 1H, Ar−H), 7.19 (d, J = 15.3 Hz, 2H, Ar−H), 7.11 (t, J = 7.4 Hz, 1H, Ar−H), 6.94 (d, J = 9.2 Hz, 1H, Ar−H), 5.32 (d, J = 6.0 Hz, 1H, p-cym−H), 5.14−5.09 (m, 2H, p-cym−H), 4.40 (d, J = 5.6 Hz, 1H, p-cym−H), 3.62 (s, 4H, O−CH_2), 3.51 (s, 2H, CH_2), 2.54 (m, 1H, p-cym−^{i}Pr), 2.48 (s, 3H, p-cym−CH_3), 2.43 (s, 4H, N−CH_2), 2.16 (s, 3H, Ar−CH_3), 1.93 (s, 3H, Ar−CH_3), 1.22 (t, J = 6.64 Hz, 6H, p-cym−^{i}Pr) (Figure S23). ^{13}C NMR (100 MHz, DMSO-d_6): δ 166.8, 158.5, 154.3, 134.8, 134.3, 129.1,128.5, 128.4, 127.3, 125.6, 124.4, 121.6, 119.5, 111.1, 102.5, 94.8, 85.7, 84.2, 82.7, 80.0, 66.2, 62.0, 30.2, 22.2, 21.8, 19.2, 17.9, 17.0 (Figure S24). IR (KBr pellets, cm^{-1}): 1615 (CH═N) (Figure S29). UV−vis [MeOH; λ_{max}, nm (ε, M^{-1} cm^{-1})]: 254 (42200), 320 (14480), 422 (3630), 479 (1910) (Figure S28). ESI-HRMS (MeOH). m/z (exp) 609.2055 (609.1995) [$Ru^{II}C_{34}H_{39}N_2O_2^+$]. Anal. Calcd for $C_{34}H_{39}ClN_2O_2Ru$: C, 63.39; H, 6.10; N, 4.35. Found: C, 63.47; H, 6.14; N, 4.39.

*Ru(p-cym)(**L6**)Cl (**6**).* Yield: 62%. ^{1}H NMR (500 MHz, DMSO-d_6): δ 7.95 (s, 1H, CH═N), 7.63 (dd, J = 19.1 and 8.5 Hz, 2H, Ar−H), 7.47 (d, J = 8.6 Hz, 1H, Ar−H), 7.28 (m, 3H, Ar−H), 7.12 (d, J = 7.4 Hz, 1H, Ar−H), 6.93 (d, J = 9.2 Hz, 1H, Ar−H), 5.40 (d, J = 6.1 Hz, 1H, p-cym−H), 5.34 (d, J = 6.2 Hz, 1H, p-cym−H), 4.97 (d, J = 5.6 Hz, 1H, p-cym−H), 4.36 (d, J = 5.7 Hz, 1H, p-cym−H), 4.08 (m, 1H, ^{i}Pr), 3.64 (s, 4H, O−CH_2), 3.58 (s, 2H, −CH_2), 3.01 (m, 1H, ^{i}Pr), 2.65−2.60 (m, 1H, p-cym−^{i}Pr), 2.44 (s, 4H, N−CH_2), 1.87 (s, 3H, Ar−CH_3), 1.42 (d, J = 6.8 Hz, 3H, ^{i}Pr), 1.33 (dd, J = 12.8 and 6.8 Hz, 6H, ^{i}Pr), 1.24 (d, J = 6.9 Hz, 3H, ^{i}Pr), 1.06 (d, J = 6.6 Hz, 3H, ^{i}Pr), 0.80 (d, J = 6.7 Hz, 3H, ^{i}Pr). ^{13}C NMR (125 MHz, DMSO-d_6): δ 167.2, 158.9, 135, 134.1, 128.6, 128.5, 127.6, 127.5, 125.7, 124.3, 124, 121.6, 118.2, 110, 102.1, 95, 86.2, 83, 82.5, 79.3, 66.2, 62.4, 53.1, 30.3, 27.3, 26.6, 26.3, 25.9, 25.8, 22.8, 22.1, 21.2, 17.1 (Figures S25−S27). IR (KBr pellets, cm^{-1}): 1590 (CH═N) (Figure S29). UV−vis [MeOH; λ_{max}, nm (ε, M^{-1} cm^{-1})]: 254 (40460), 322 (3160), 429 (3490), 494 (1730) (Figure S28). ESI-HRMS (MeOH). m/z (exp) 665.2681 (665.2664) [$Ru^{II}C_{38}H_{47}N_2O_2^+$]. Anal. Calcd for $C_{38}H_{47}ClN_2O_2Ru$: C, 65.17; H, 6.76; N, 4.00. Found: C, 65.32; H, 6.72; N, 4.08.

X-ray Crystallography. Single crystals of complexes **1**−**6** were obtained from a methanolic solution of the respective complexes by slow evaporation at 25 °C. All of the solutions were kept in the dark during the slow evaporation process to obtain crystals. Good-quality single crystals suitable for diffraction were mounted over a loop of the goniometer of a SuperNova, Dual, Cu at zero, Eos diffractometer. The data of the crystals were collected at 100(1) K to enhance the stability

https://doi.org/10.1021/acs.inorgchem.1c01363
Inorg. Chem. XXXX, XXX, XXX−XXX

of the crystal during diffraction and minimize the probability volume of the thermal ellipsoids. Cu Kα was used as the X-ray source for data collection due to the nonavailability of Mo Kα. Data reduction was done using the *CrysAlisPro171.37.33c* software. The reduced data were then taken to solve the structure using the *ShelXT* structure solution program and consecutively refined with the *ShelXL* refinement package using least-squares minimization in *Olex2*. The structures were deposited to the CCDC database, and the deposition numbers are 2081907−2081911.

Solution Stability Study. ^{1}H NMR studies were performed at different time points at 25 °C for a period of 24 h to estimate the stability of the complexes in solution. The solution composed of 3:7 (v/v) dimethyl sulfoxide (DMSO)-d_6/20 mM phosphate buffer at pH* 7.4 (pH meter reading without correction for the effects of D on the glass electrode) and 4 mM NaCl in D_2O at 25 °C.

Distribution Coefficient Determination. The standard shake-flask method with an octanol/water mixture following OECD guidelines[80] led to determination of the distribution coefficient (log $D_{o/w}$) of the complexes. A known amount of complex was solubilized with *n*-octanol presaturated with a 130 mM NaCl solution. The solution was continuously shaken at 25 °C on an orbital shaker for 12 h, followed by centrifugation of the biphasic solution for 3 min, to allow complete phase separation. The aliquot from each layer was measured separately in a UV−vis spectrophotometer with the appropriate dilution. Each complex was measured in triplicate. The concentrations of the complexes were calculated from the molar extinction coefficient, and their ratios provided the distribution coefficient (log $D_{o/w}$).

Cell Lines and Culture Condition. The cells were grown in a 100 mm Petri dish with an adherent monolayer and maintained at the logarithmic phase in a 5% CO_2 atmosphere using the appropriate culture media, supplemented with 10% fetal bovine serum (FBS; Gibco) and a 1× antibiotic−antimycotic solution. Hep-G2 was grown in Minimal Essential Medium, while MiaPaCa2 and MDA-MB-231 were cultured in Dulbecco's Modified Eagle Medium (DMEM) and in a 1:1 mixture of DMEM with Ham's F12 nutrient mixture (i.e., DMEM/F-12), respectively.

Cell Viability Assay. The effect of the complexes on the growth inhibition of the tumor cell lines (MDA-MB-231, Hep-G2, and MiaPaCa2) was assessed with MTT assay. About 6×10^3 cells were added in each well of a 96-well plate in the appropriate medium (200 μL) and incubated at 37 °C in a 5% CO_2 atmosphere. After incubation for 24 h, the medium was removed, and fresh medium (200 μL) was added. The compound to be tested was added at different concentrations in the wells. The compounds were solubilized in DMSO and added to the respective media such that the concentration of DMSO in the well was less than 0.2%. Oxaliplatin was solubilized in *N*,*N*-dimethylformamide (DMF) and added to the respective media such that the concentration of DMF in well was less than 0.2%. Upon incubation at 37 °C for 72 h, the medium was removed and renewed with a fresh medium (200 μL) containing 0.1 mg mL^{-1} MTT. After 3 h of incubation at 37 °C, the medium was replaced with 200 μL of DMSO. The inhibitory effect on the cells was calculated by measuring the absorbance of the drug-treated cells to the untreated ones at 570 nm using a Biotech SYNERGY H1M microplate reader. Each assay was performed in triplicate. IC_{50} values (the drug concentration at which 50% of the cell growth is inhibited) were calculated by fitting curves with nonlinear regression in *GraphPad Prism 5*, version 5.03, by plotting the percent of cell viability versus the logarithm of the drug concentration in micromolar.

Detection of Apoptosis: PE-Annexin-V/7-AAD Assay. Apoptosis of cells was detected using the PE-Annexin-V and 7-AAD dual staining apoptosis detection kit (BD Pharmingen) by flow cytometry according to the manufacturer's protocol. About 1×10^5 MDA-MB-231 cells were seeded in a 6-well plate and incubated for 72 h at 37 °C in a 5% CO_2 atmosphere. Subsequently, the cells were treated with complexes **3**−**5** for 8 h with a IC_{50} solution concentration. Treated and untreated cells were then harvested with ice-cold 1× phosphate-buffered saline (PBS) containing 0.1 mM ethylenediaminetetraacetic acid, subsequently washed with cold 1 × PBS twice, and finally resuspended in an Annexin-V binding buffer. Cells were then incubated with both PE-Annexin-V and 7-AAD for 15 min in the dark at 25 °C. Data were analyzed in a BD Biosciences FACS Calibur flow cytometer within 1 h of sample preparation.

Acridine Orange (AO) Assay. About 5×10^4 MDA-MB-231 cells were seeded in a 30 mm glass bottom Petri dish and incubated up to 70% confluency at 37 °C in a 5% CO_2 atmosphere. Then the medium was renewed and treated with complexes **2** and **6** at IC_{50} for 2.5 h. Then the medium was removed, and the cells were washed with 1× PBS twice and incubated with AO (2 μM) in the medium for 15 min at 37 °C in a 5% CO_2 atmosphere. AO was removed, and the cells were washed with 1× PBS twice and visualized under a confocal laser scanning microscope (Leica TCS SP8). Excitation was at 488 ± 10 nm, and emissions were collected at 520 ± 20 nm (green) and 625 ± 20 nm (red).

Immunofluorescence. About 5×10^4 cells of MDA-MB-231 were seeded in 24-well plates over a glass coverslip and incubated up to 70% confluency. The cells were treated with complexes **2** and **6** at IC_{50} for 6, 12, and 24 h at 37 °C in a 5% CO_2 atmosphere. Then media containing drugs were removed and washed with ice-cold 1× PBS twice. The cells were fixed with a 2% (v/v) paraformaldehyde solution for 20 min and quenched with 50 mM ammonium chloride for 20 min. The cells were washed with 1× PBS twice and blocked with 1% bovine serum albumin (BSA) and 0.075% saponin in 1× PBS for 1 h at room temperature. Following blocking, the cells were washed once with 1× PBS and incubated with the primary anti-LAMP1 antibody (antihuman Lamp1, mouse monoclonal antibody, H4A3, and DSHB) and anti-LAMP2 antibody (DSHB and H4B4) and mouse monoclonal anti-cathepsin D antibody (BD Biosciences C47620) in 0.5% BSA for 2 h in a humid chamber at room temperature. This step was further followed by three washes with 1× PBS. The cells were incubated with the highly cross-adsorbed secondary antibody donkey anti-mouse IgG (H+L; Alexa Fluor 568, Invitrogen A10037) and Phalloidin-iFluor647 (Abcam ab176759) in 0.5% BSA in 1 × PBS for 1 h 30 min at room temperature in a humid chamber, washed with 1× PBS twice, mounted on slides using 4′,6-diamidino-2-phenylindole (DAPI)-containing mounting media (Fluoroshield with DAPI, F6057, Sigma-Aldrich), and imaged under a confocal laser scanning microscope (Leica TCS SP8). Emission was collected at 568 nm upon excitation at 552 nm.

Immunoblot Assay. MDA-MB-231 cells were grown in DMEM-F12 supplemented with 10% FBS and antibiotics at 37 °C and 5% CO_2. To test the effect of complexes **2** and **6** on lysosomal degradation, we checked the expression level of the lysosomal membrane proteins (LAMP1), the autophagy markers (LC3B), and the level of mTORC1 downstream effectors (phospho-p70S6K/total p70S6K). The cells were grown up to 70% confluency and treated with a IC_{50} dose of complexes **2** and **6** for 2, 6, and 12 h. The cells were lysed using a RIPA lysis buffer, and the protein samples were resolved by running through sodium dodecyl−sulfate polyacrylamide gel electrophoresis. The protein was transferred to a nitrocellulose membrane and blocked with 5% skim milk in 1× TBST (a mixture of tris-buffered saline and Tween 20) for 2 h at room temperature. After blocking, the membrane was incubated with a primary antibody diluted in 3% skim milk in 1× TBST overnight at 4 °C. Following primary antibody incubation, the membrane was washed with 1× TBST and the protein abundance of the respective markers was detected using a horseradish peroxidase-conjugated secondary antibody.

RESULTS AND DISCUSSION

Synthesis and Characterization. The N,O-coordinating ligands **HL1**−**HL6** were prepared by refluxing the respective amine and aldehyde in MeOH for 24 h. The product was obtained either by precipitation or by column chromatography (silica gel 60−120 mesh). The ruthenium(II) *p*-cymene complexes **1**−**6** were synthesized by stirring the ligands with 1 equiv of KOH, followed by the addition of $Ru_2(p\text{-cym})_2Cl_4$ in MeOH at 25 °C for 12−18 h, as shown in Scheme 1. The

https://doi.org/10.1021/acs.inorgchem.1c01363
Inorg. Chem. XXXX, XXX, XXX−XXX

Scheme 1. Synthesis of Ligands HL1−HL6 and Ruthenium Complexes 1−6

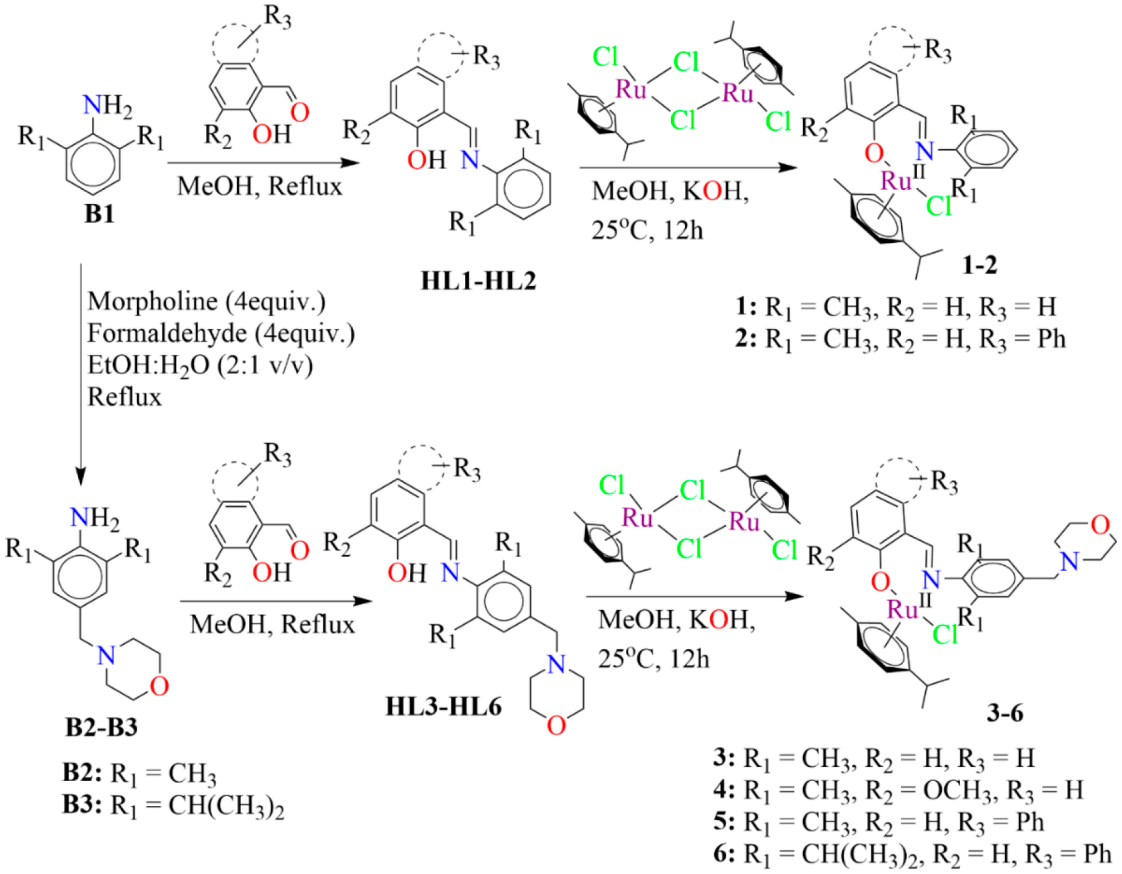

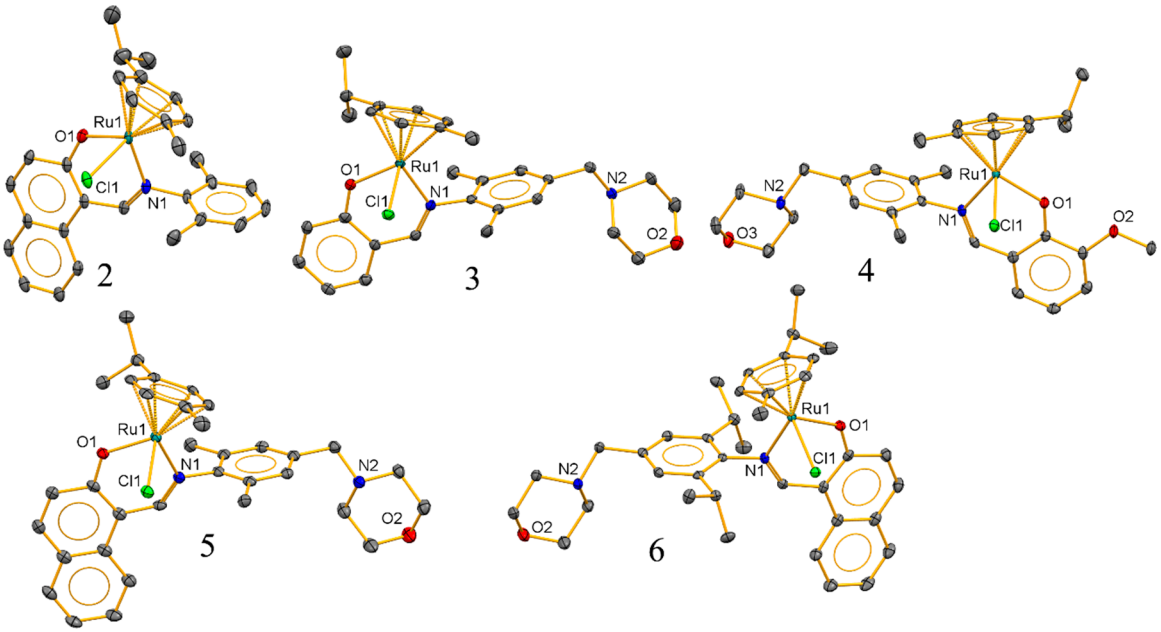

Figure 2. ORTEP diagrams of the molecular structures of complexes **2**−**6**. Thermal ellipsoids are drawn at the 50% probability level. All H atoms are omitted for clarity.

product was isolated in pure form by column chromatography in neutral alumina. The complexes presented are new, and all of them are well-characterized by ^{1}H and ^{13}C NMR, ESI-HRMS, FT-IR, and UV−vis analysis. Complexes **2**−**6** are also characterized by single-crystal X-ray crystallography. The UV−vis spectra suggest that there are $\pi-\pi^*$ and ligand-to-metal charge-transfer transitions ca. 290−321, 405−435, and 460−495 nm, respectively (Figure S28). The IR data show that the stretching frequency for the imine bonds is 1580−1615 cm^{-1} for **1**−**6** (Figure S29).

https://doi.org/10.1021/acs.inorgchem.1c01363
Inorg. Chem. XXXX, XXX, XXX−XXX

Table 1. Selected Bond Lengths (Å) of Complexes 2−6

2		3		4	
Ru1−Cl1	2.424(2)	Ru1−Cl1	2.418(1)	Ru1−Cl1	2.427(1)
Ru1−O1	2.056(2)	Ru1−O1	2.053(2)	Ru1−O1	2.070(1)
Ru1−N1	2.100(2)	Ru1−N1	2.096(2)	Ru1−N1	2.110(2)
Ru1−C20	2.192(3)	Ru1−C21	2.199(3)	Ru1−C22	2.201(2)
Ru1−C21	2.196(3)	Ru1−C22	2.202(3)	Ru1−C23	2.198(2)
Ru1−C22	2.179(3)	Ru1−C23	2.176(3)	Ru1−C24	2.179(2)
Ru1−C23	2.217(3)	Ru1−C24	2.236(3)	Ru1−C25	2.210(2)
Ru1−C24	2.194(3)	Ru1−C25	2.192(3)	Ru1−C26	2.175(2)
Ru1−C25	2.185(3)	Ru1−C26	2.198(3)	Ru1−C27	2.194(2)
5				6	
Ru1−Cl1	2.432(6)			Ru1−Cl1	2.418(5)
Ru1−O1	2.054(2)			Ru1−O1	2.058(1)
Ru1−N1	2.101(2)			Ru1−N1	2.090(2)
Ru1−C25	2.215(2)			Ru1−C29	2.215(2)
Ru1−C26	2.178(2)			Ru1−C30	2.189(2)
Ru1−C27	2.180(2)			Ru1−C31	2.214(2)
Ru1−C28	2.202(2)			Ru1−C32	2.201(2)
Ru1−C29	2.209(2)			Ru1−C33	2.180(2)
Ru1−C30	2.189(2)			Ru1−C34	2.176(2)

Table 2. Selected Bond Angles (deg) of Complexes 2−6

2		3		4	
O1−Ru1−Cl1	83.00(6)	O1−Ru1−Cl1	82.92(6)	O1−Ru1−Cl1	84.31(4)
O1−Ru1−N1	86.90(6)	O1−Ru1−N1	87.42(9)	O1−Ru1−N1	87.68(6)
N1−Ru1−Cl1	86.90(6)	N1−Ru1−Cl1	85.82(6)	N1−Ru1−Cl1	85.93(4)
O1−Ru1−C20	87.90(10)	O1−Ru1−C21	86.13(10)	O1−Ru1−C22	86.25(6)
O1−Ru1−C21	112.93(10)	O1−Ru1−C22	93.88 (10)	O1−Ru1−C23	95.45 (6)
O1−Ru1−C22	150.57(10)	O1−Ru1−C23	124.50(10)	O1−Ru1−C24	126.97(6)
O1−Ru1−C23	159.46(10)	O1−Ru1−C24	161.45(10)	O1−Ru1−C25	163.86(6)
O1−Ru1−C24	121.78(10)	O1−Ru1−C25	146.31(10)	O1−Ru1−C26	144.05(7)
O1−Ru1−C25	93.29(10)	O1−Ru1−C26	108.95(10)	O1−Ru1−C27	107.31(6)
5				6	
O1−Ru1−Cl1	82.92(6)			O1−Ru1−Cl1	84.25(5)
O1−Ru1−N1	87.42(9)			O1−Ru1−N1	86.43(6)
N1−Ru1−Cl1	85.82(6)			N1−Ru1−Cl1	84.60(5)
O1−Ru1−C25	95.71(8)			O1−Ru1−C29	93.82(7)
O1−Ru1−C26	127.24(8)			O1−Ru1−C30	88.05(7)
O1−Ru1−C27	164.19(8)			O1−Ru1−C31	110.04(7)
O1−Ru1−C28	144.46(8)			O1−Ru1−C32	146.84(7)
O1−Ru1−C29	108.13(8)			O1−Ru1−C33	162.04(8)
O1−Ru1−C30	87.71(8)			O1−Ru1−C34	124.28(8)

X-ray Crystallography. Single crystals of each complex were obtained from a methanolic solution of the complexes following a slow evaporation method. Complexes **2**−**4** crystallized in a monoclinic system with space group $P2_1/c$, whereas complexes **5** and **6** crystallized in a triclinic system with $P\bar{1}$ space group. The crystal structure of each complex showed a chelating N,O coordination bond from the bidentate Schiff base ligands and monodentate coordination by chloride (Figure 2). The fourth position was occupied by a *p*-cymene ring coordinating with the Ru center in an η^6 fashion. Thus, the Ru^{II} centers in these complexes are in a pseudooctahedral geometry (Figure 2). In complexes **2**−**4**, each unit cell contained four complexes, whereas for complexes **5** and **6**, the unit cell contained two complexes. Some important bond distances, angles and crystallographic parameters are listed in Tables 1−3. The Ru−Cl bond distances of the complexes range between 2.42 and 2.43 Å, which may be considered marginally longer than the Ru−Cl distances of ca. 2.39−2.41 Å observed for our earlier reported N,N-coordinated complexes.[9,81,82] The Ru−O bond distances of the complexes range between 2.06 and 2.07 Å, and the Ru−C bond lengths of *p*-cymene are in the range of 2.18−2.21 Å (Table 2). The distance between the centroid of the *p*-cymene ring and Ru^{II} in the 2,6-diisopropylaniline-based N,N-coordinated complex is ca. 1.70 Å,[83] whereas in our complexes, it is ca. 1.68 Å; thus, the interaction between *p*-cymene and Ru^{II} is stronger in the N,O-coordinated complexes. In complexes **3**−**6**, weak intermolecular hydrogen bonding is present, displaying D···A distances of 3.4−3.8 Å with a ∠D−H···A of 138−162°, between a Ru^{II}-coordinated Cl atom and an aromatic H atom of the *p*-cym attached to a Ru^{II} from a neighboring complex. Another intermolecular weak hydrogen-bonding interaction is present in **3**, **5**, and **6** among a Ru-coordinated O atom and an aromatic H atom of *p*-cym within the range of 3.2−3.4 Å (D···

https://doi.org/10.1021/acs.inorgchem.1c01363
Inorg. Chem. XXXX, XXX, XXX−XXX

Table 3. Selected Crystallographic Parameters for Complexes 2−6

	2	3	4	5	6
empirical formula	$C_{29}H_{30}ClNORu$	$C_{30}H_{37}ClN_2O_2Ru$	$C_{31}H_{39}ClN_2O_3Ru$	$C_{34}H_{39}ClN_2O_2Ru$	$C_{38}H_{47}ClN_2O_2Ru$
radiation	Cu Kα (λ = 1.54184)	Cu Kα (λ = 1.54184)	Cu Kα (λ = 1.54184)	Cu Kα (λ = 1.54184)	Cu Kα (λ = 1.54184)
fw/(g/mol)	545.06	594.13	624.16	644.19	700.326
temp/K	100.00(10)	94.8(4)	100.00(10)	100.00(10)	101(2)
cryst syst	monoclinic	monoclinic	monoclinic	triclinic	triclinic
space group	$P2_1/c$	$P2_1/c$	$P2_1/c$	$P\bar{1}$	$P\bar{1}$
a/Å	7.96410(10)	8.8322(3)	9.5488(2)	10.7783(5)	11.0249(5)
b/Å	17.0207(3)	14.4477(5)	14.0931(3)	10.8455(5)	11.7028(5)
c/Å	17.4922(3)	21.3187(7)	21.2814(4)	13.4383(5)	13.9028(4)
α/deg	90	90	90	85.531(4)	83.556(3)
β/deg	92.9190	98.241(4)	92.943(2)	83.630(4)	89.613(3)
γ/deg	90	90	90	69.294(4)	69.622(4)
volume/Å^3	2368.07(7)	2692.28(16)	2860.11(10)	1459.08(12)	1669.88(12)
Z	4	4	4	2	2
ρ_{calc}/(mg/cm^3)	1.529	1.466	1.450	1.466	1.393
μ/mm^{-1}	6.561	5.856	5.568	5.452	4.808
F(000)	1120.0	1232.0	1296.0	668.0	732.0
cryst size/mm^3	0.3647 × 0.2192 × 0.0624	0.111 × 0.0468 × 0.0213	0.4614 × 0.2865 × 0.1352	0.1333 × 0.1333 × 0.0582	0.125 × 0.125 × 0.0480
2θ range for data collection/deg	7.252−132.336	7.416−132.42	7.526−132.158	6.624−132.266	6.402−132.418
index ranges	$-9 \le h \le 9$, $-20 \le k \le 18$, $-20 \le l \le 20$	$-8 \le h \le 10$, $-17 \le k \le 11$, $-24 \le l \le 25$	$-10 \le h \le 11$, $-16 \le k \le 15$, $-23 \le l \le 25$	$-11 \le h \le 12$, $-12 \le k \le 12$, $-15 \le l \le 15$	$-12 \le h \le 13$, $-13 \le k \le 13$, $-16 \le l \le 16$
reflns collected	41894	11310	11725	10491	13122
indep reflns	4142 [R_{int} = 0.0472, R_σ = 0.0178]	4695 [R_{int} = 0.0392, R_σ = 0.0472]	4970 [R_{int} = 0.0247, R_σ = 0.0274]	5063 [R_{int} = 0.0282, R_σ = 0.0347]	5716 [R_{int} = 0.0369, R_σ = 0.0424]
data/restraints/ param	4142/0/303	4695/0/330	4970/0/349	5063/0/366	5716/0/404
GOF on F^2	1.068	1.033	1.063	1.059	1.023
final R indexes [$I \ge 2\sigma$ (I)]	R_1 = 0.0305, wR_2 = 0.0748	R_1 = 0.0334, wR_2 = 0.0785	R_1 = 0.0241, wR_2 = 0.0611	R_1 = 0.0288, wR_2 = 0.0723	R_1 = 0.0270, wR_2 = 0.0650
final R indexes [all data]	R_1 = 0.0314, wR_2 = 0.0754	R_1 = 0.0393, wR_2 = 0.0820	R_1 = 0.0250, wR_2 = 0.0617	R_1 = 0.0310, wR_2 = 0.0740	R_1 = 0.0301, wR_2 = 0.0664
largest diff peak/hole/(e /Å^3)	0.99/−0.64	0.89/−0.95	0.37/−0.70	1.47/−0.77	0.42/−0.65

[a] $R_1 = \sum||F_o| - |F_c||/\sum|F_o|$. [b] $wR_2 = [\sum[w(F_o^2 - F_c^2)^2]/\sum w(F_o^2)^2]^{1/2}$.

A) with a ∠D−H···A of ca. 142−175°. In **4**, a weak hydrogen-bonding interaction is present among an O atom of methoxy and an aromatic H atom of *p*-cym having a distance of ∼3.4 Å (D···A) with a ∠D−H···A of ca. 143°. In **2**, a weak hydrogen-bonding interaction is present between the Ru-coordinated Cl atom and aromatic H atom with a distance of ca. 3.7 Å (D···A) and a ∠D−H···A of ca. 153−156°. Besides, a weak $\pi\cdots\pi$-stacking interaction is also observed in complex **2** (Figure S30).

Stability in Solution. The solution stability of the complexes was investigated to understand whether the complexes dissociate or hydrolyze to monoaquated species in solution over time. The solution stability was measured at a physiological pH of 7.4 in a 20 mM phosphate buffer having 4 mM NaCl and mixed with DMSO-d_6 in a 7:3 (v/v) ratio. Two complexes were investigated to represent the solution stability. These complexes, **3** and **4**, hydrolyzed immediately upon dissolution to form the monoaquated complex releasing the halide (Figure 3). The immediate hydrolysis was confirmed by matching the chemical shifts of the aforementioned sample with a sample incubated with 1 equiv of $AgNO_3$ to precipitate AgCl and lead to the monoaquated complex. The sample without added $AgNO_3$ and with $AgNO_3$ showed the exact same chemical shifts, confirming the immediate hydrolysis (Figure 3). The hydrolyzed complexes are stable for at least 24 h (time-dependent NMR was done only for a 24 h period). We also investigated the stability of complex **4** as a representative in the series for up to 72 h through ^{1}H NMR and found that it is mostly intact even upon 72 h of incubation (Figure S32).

Complexes **2**, **5**, and **6** are also hydrolyzed immediately (Figure S31), but they have poor solubility in the concentrations (ca. 2 mM) used for NMR and precipitate after 1 h. In order to understand whether this was due to coordination with inorganic phosphate, we investigated the precipitate obtained from the most active complex **6**, which was soluble in MeOH, and studied its ESI-MS, but we found the monopositive dehalogenated complex [Ru(*p*-cym)(**L6**)]$^+$ at m/z 665.2697 (calcd 665.2676) and the dipositive dehalogenated complex [Ru(*p*-cym)(**HL6**)]$^+$ at m/z 333.1382 (calcd 333.1374) (Figure S33). The ^{31}P NMR of the precipitate did not provide any P signal from the precipitate in CD_3OD. One reason could be that the precipitate does not have a good solubility. The ESI-MS study of the precipitate did provide a small peak at m/z 850.3422 corresponding to a monomeric ruthenium distribution, but the peak could not be assigned to any phosphate adduct.

Distribution Coefficient Determination. Lipophilicity is an important property of a drug for its absorption, distribution, potency, and elimination. The lipophilicity was determined

https://doi.org/10.1021/acs.inorgchem.1c01363
Inorg. Chem. XXXX, XXX, XXX−XXX

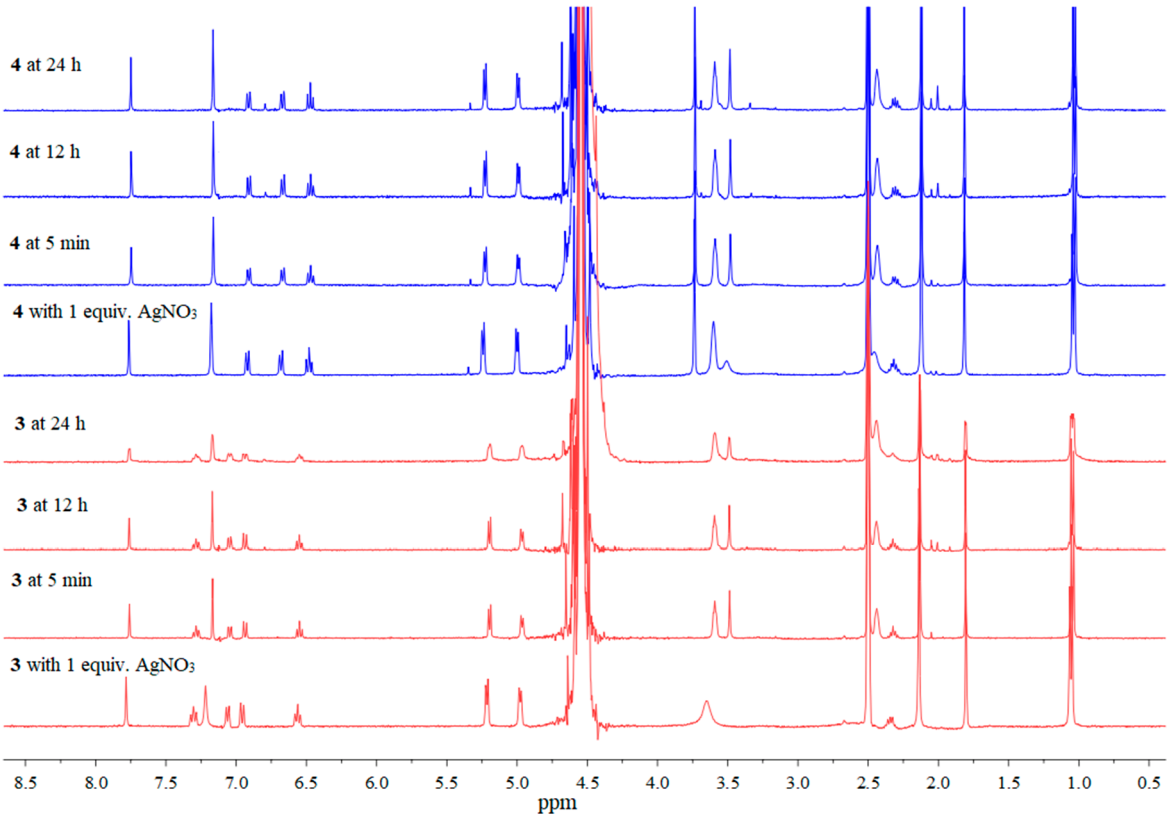

Figure 3. Stability of **3** and **4** in a 20 mM phosphate buffer (pH* 7.4) with 4 mM NaCl and 30% DMSO-d_6.

with the standard shake-flask method in *n*-octanol and water as per the OECD guidelines.[80,84] The log *D* values of complexes **1**−**6** decreased in the presence of the pendant morpholine compared to the otherwise same complexes without the morpholine motif (Figure 4). Thus, the presence of morpholine increases the water solubility. The log *D* continuously increases for **3**−**6** because of an increase in the presence of hydrophobic motifs (viz. naphthyl and isopropyl groups). All of the complexes exhibit positive log *D* values in the range of ca. 0.6−2.2, suggesting that the lipophilicity is well within the required limits as per Lipinski's rule of five.

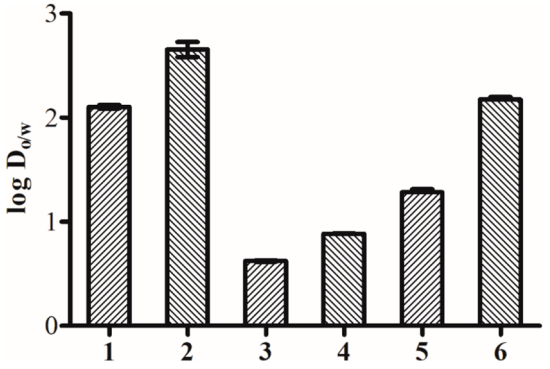

Figure 4. Lipophilicity of complexes **1**−**6** in a 1:1 (v/v) octanol and water mixture at 25 °C.

Antiproliferative Activity. The in vitro antiproliferative activity of complexes **1**−**6** was tested in three different cell lines by MTT assay under normoxic conditions. The cell lines chosen were triple-negative human metastatic breast adenocarcinoma (MDA-MB-231), human pancreatic carcinoma (MiaPaCa2), and hepatocellular carcinoma (Hep-G2), all of which belong to the category of cancers that are relatively difficult to cure. A comparison of the antiproliferation data between the complexes with and without the morpholine motif of the otherwise same ligands, e.g., complexes **1** and **3**, shows that the nonmorpholine-based **1** is more active than the corresponding pendant morpholine bearing **3** (Table 4). The difference in the antiproliferative activity minimizes when we compare **2** and **5**. Both **2** and **5** show comparable activity in MDA-MB-231 and Hep-G2, but **5** is more active in MiaPaCa2.

Table 4. In Vitro Anticancer Activity of Complexes 1−6 in Various Cancer Cell Lines under Normoxic Conditions

	IC_{50}[a] ± SD[b] (μM)		
compound	MDA-MB-231	Hep-G2	MiaPaCa2
HL1	>50	ND	ND
1	1.9 ± 0.4	5.8 ± 0.9	3.6 ± 0.3
HL2	>50	ND	ND
2	1.6 ± 0.3	4.1 ± 0.5	3.1 ± 0.3
HL3	>100	ND	ND
3	4.4 ± 0.4	13.9 ± 1.9	8.4 ± 1.6
HL4	>100	ND	ND
4	3.0 ± 0.8	9.1 ± 2.2	7.3 ± 2.1
HL5	>50	ND	ND
5	1.5 ± 0.3	4.4 ± 0.4	2.0 ± 0.6
HL6	>50	ND	ND
6	1.2 ± 0.3	2.8 ± 0.1	2.0 ± 0.2
oxaliplatin	19.2 ± 1.2[27]	9.8 ± 0.3	5.7 ± 0.2

[a]MTT assay was performed in normoxic conditions after 72 h of incubation. [b]Standard deviation.

https://doi.org/10.1021/acs.inorgchem.1c01363
Inorg. Chem. XXXX, XXX, XXX−XXX

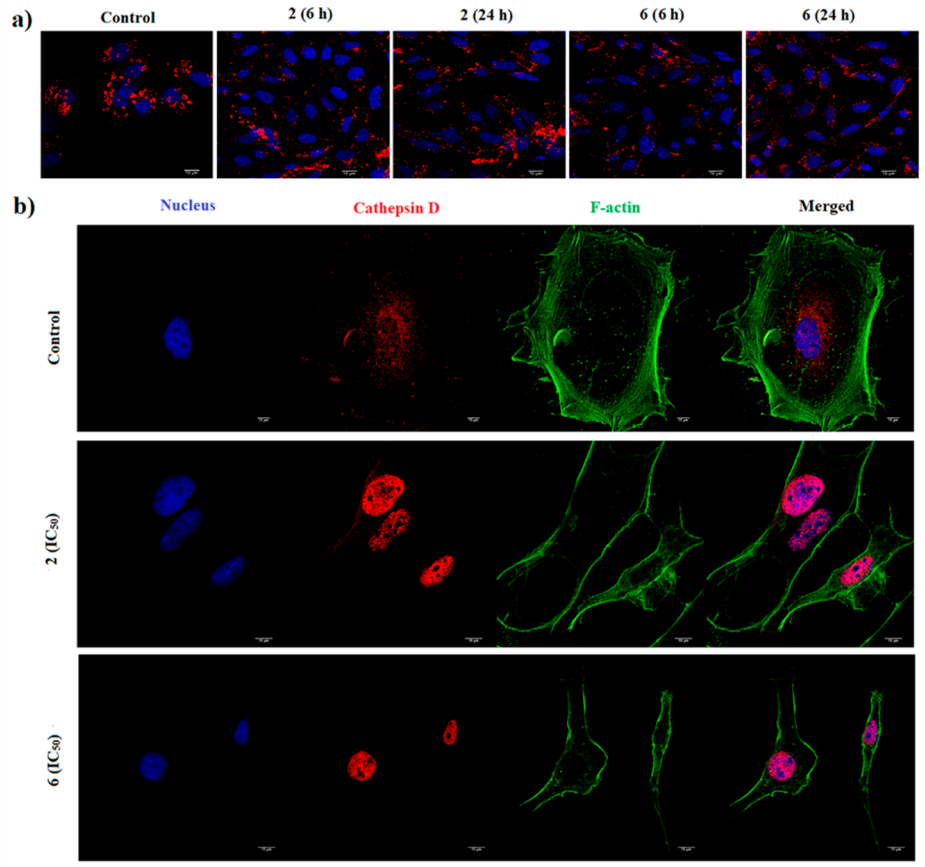

Figure 5. (a) Distribution of LAMP-2 in the MDA-MB-231 cells after incubation with **2** and **6** after 6 and 24 h. (b) Immunofluorescence study of cathepsin D after incubation with IC_{50} doses of **2** and **6** for 4 h.

Complex **6**, which is more hydrophobic (Figure 4), shows the highest effect (IC_{50} = ca. 1.2−2.0 μM) in the series (Figures S34−S37). Complexes **2**, **5**, and **6** were also investigated in the nontumorigenic cell line HEK293 to see if they are less toxic to other cells. The IC_{50} values obtained are 1.7 ± 0.3, 1.5 ± 0.3, and 1.4 ± 0.2 μM for **2**, **5**, and **6**, respectively (Figure S37), suggesting that they are also toxic to noncarcinogenic cells like cisplatin or oxaliplatin. Notably, most of the complexes require lower doses than the oxaliplatin in killing the same cancer cells. Complex **6** is ca. 9 times more effective against the TNBC, MDA-MB-231, compared to oxaliplatin. It is evident that the presence of the naphthyl group and diisopropyl substitution in the aniline is more important in enhancing the antiproliferative activity and lipophilicity.

Investigation of the lysosomal role in the pathway of cell killing. The complexes were designed with or without morpholine as pendant motifs so lysosome membrane permeabilization was studied. MDA-MB-231 cells were stained with AO for monitoring the fate of the acidic lysosomal vesicles. The red puncta for control imply the presence of acidic vesicles (viz. lysosomes), and after 2.5 h treatment with complexes **2** and **6**, the red dots remained (Figure S38b), which implies that the lysosomes remained acidic. The lysosomal membrane has a lipid bilayer that contain glycoproteins. The most abundant lysosomal membrane proteins are lysosome-associated membrane proteins 1 and 2 (LAMP-1 and LAMP-2).[85,86] The inner lumen of these proteins is highly glycosylated and protects the lysosomal membrane from the digestive enzymes. If the complexes disrupt the lysosomal membrane integrity and breaks them into smaller vesicles, then the intracellular distribution of LAMP-1 or LAMP-2 would be different from the control, but as displayed in Figure 5a, the distribution remains almost comparable to that of untreated control cells. When the MDA-MB-231 cells are incubated with **2** and **6** at IC_{50} doses for 24 h, the LAMP-2 population seems not to differ too much to show a higher dispersion in the cytosol compared to the control. The above result implies that the lysosomal membrane integrity is preserved. However, the compound-treated cells show cathepsin D translocation to the nucleus (Figure 5b). So, there is a release of cathepsin D from the lysosomes as a result of treatment of the complexes, and it translocates to the nucleus. It is well-known that the release of cathepsins in cytosol may lead to caspase-dependent or -independent cell killing by apoptosis or necrosis.[87]

To understand whether the ruthenium(II) complexes (viz. **2** and **6**) are affecting the formation and activation of signaling complexes on the lysosomal membrane, we investigated expression of the downstream effectors of active mTORC1 in MDA-MB-231 cells treated with **2** and **6**. It is known that the activation of mTORC1 leads to phosphorylation of ribosomal protein S6 kinase (p70S6K) and the phosphorylated p70S6K regulates cell growth, proliferation, and protein synthesis.[88,89] The ratio phosphorylated p70S6K to the total cellular pool of p70S6K is indicative of the mTORC1 activity. Our results show that the expression is not changed (Figure S38c) upon treatment with the complexes. Furthermore, we also investigated whether autophagy is activated by the

https://doi.org/10.1021/acs.inorgchem.1c01363
Inorg. Chem. XXXX, XXX, XXX−XXX

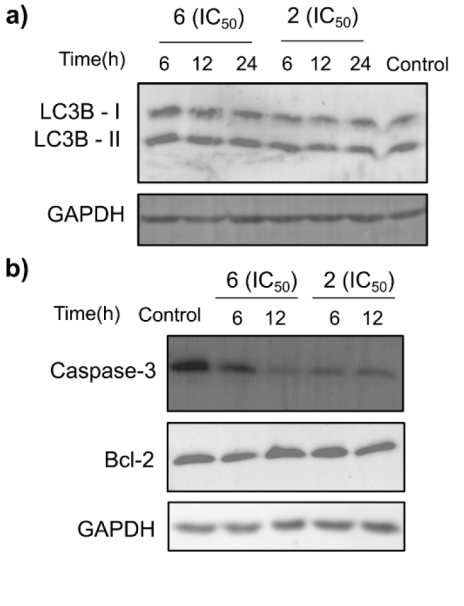

c)

	Live Cells (%)	Early Apoptotic Cells (%)	Late Apoptotic Cells (%)	Dead/ Necrotic Cells (%)
Control	94.16	0.71	3.66	1.47
3 (IC_{50})	73.18	1.48	16.10	9.25
4 (IC_{50})	75.77	0.86	13.01	10.36
5 (IC_{50})	66.5	0.93	19.95	12.62

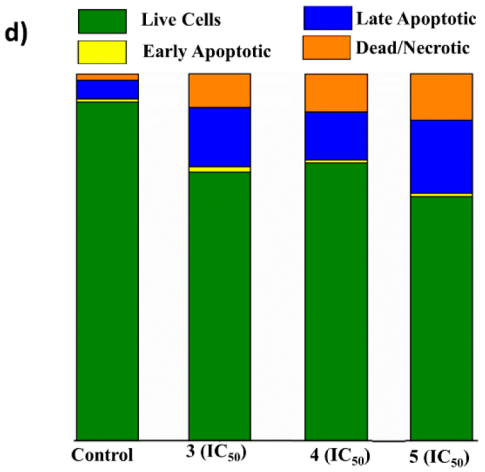

Figure 6. (a) Expression of LC3B in MDA-MB-231 cell lines after incubation with **2** and **6** for 6, 12, and 24 h. (b) Expression of caspase-3, Bcl-2, and Bid in MDA-MB-231 cell lines after incubation with **2** and **6** for 6 and 12 h. (c) Tabular representation of the induction of apoptosis and necrosis by **3**−**5** in MDA-MB-231 cells. (d) Bar diagram of the induction of apoptosis and necrosis by **3**−**5** in MDA-MB-231 cells.

complexes by investigating expression of LC3B. During autophagy, LC3B-I is converted to LC3B-II,[90−96] so the increased ratio of LC3B-II to LC3B-I would indicate autophagic induction. In our case, the ratio remains the same, suggesting that autophagy is not initiated (Figure 6a). Because the complexes are not targeting autophagic cell death, we monitored the mitochondrial Bcl-2, which is a regulator protein localized in the outer mitochondrial membrane to regulate apoptosis.[97−99] However, Bcl-2 abundance remains unaltered in cells treated with the compound (Figure 6b) for both complexes, suggesting that mitochondria-mediated apoptosis may not be happening. This was further confirmed when we investigated caspase-3-mediated apoptosis. The immunoblot results show that the activation of caspase-3 did not take place but rather active caspase-3 is absent (Figure 6b) in cells treated with **2** and **6**, suggesting that the cell death is caspase-independent. The cell death pathway was further investigated by PE-Annexin-V and 7-AAD double staining assay in MDA-MB-231 cells for **3**−**5** using flow cytometry. Treatments of 8 h with IC_{50} doses of **3**−**5** induced ∼13%, ∼10%, and ∼17% late apoptosis and ∼8%, ∼9%, and ∼11% necrotic/dead cells, respectively (Figures 6c,d and S39), thus indicating that caspase-independent apoptosis and necrotic cell death is the probable cell killing pathway for these complexes. This is a major change in the pathway of action from our earlier-reported complexes of the same genre.[11,81] Complexes **3**−**5** have the morpholine motif attached to the 2,6-disubstituted anilines, but complex **2** does not have the pendant morpholine but also does not activate caspase-3 (Figure 6b) and translocate cathepsin D to the nucleus (Figure 5b). Thus, irrespective of the presence of the morpholine motif, the combination of the aldehyde and the disubstituted anilines renders ruthenium(II) *p*-cymene complexes that induce a caspase-independent apoptosis and necrotic pathway of cell killing.

CONCLUSIONS

The N,O-coordinating 2,6-disubstituted aniline-based Schiff bases form ruthenium(II) *p*-cymene complexes that immediately hydrolyze in solution to form monoaquated complexes stable at pH 7.4 for at least 24 h. The presence or absence of the pendant morpholine conjugated to the aniline did not improve the antiproliferative activity, which is evident from the similarity of the dosage required for complexes **2** and **5**. These complexes do not seem to dismantle the lysosome, but their presence leads to translocation of cathepsin D, which is not dependent on the presence of the morpholine in the ligand. The complexes display high cytotoxicity to the cancer cells. However, the cytotoxicity is not mediated by autophagy or caspase-dependent apoptosis, but rather caspase-independent apoptosis and necrosis are the possible pathways, as is evident from the immunoblotting and flow cytometry studies.

ASSOCIATED CONTENT

Supporting Information

The Supporting Information is available free of charge at https://pubs.acs.org/doi/10.1021/acs.inorgchem.1c01363.

NMR spectra of ligands (Figures S1−S12) and complexes (Figures S13−S27), UV−vis spectra of the complexes (Figure S28), IR spectra of the complexes (Figure S29), interaction of the crystals in the unit cell (Figure S30), aquation of **2**, **5**, and **6** (Figure S31), aquation of **4** up to 72 h (Figure S32), ESI-MS spectrum of the precipitate of complex **6** obtained from an NMR tube during time-dependent stability (Figure S33), MTT assay (Figures S34−S37), investigation of lysosomal changes (Figure S38), and investigation of apoptosis (Figure S39) (PDF)

https://doi.org/10.1021/acs.inorgchem.1c01363
Inorg. Chem. XXXX, XXX, XXX−XXX

Accession Codes

CCDC 2081907−2081911 contain the supplementary crystallographic data for this paper. These data can be obtained free of charge via www.ccdc.cam.ac.uk/data_request/cif, or by emailing data_request@ccdc.cam.ac.uk, or by contacting The Cambridge Crystallographic Data Centre, 12 Union Road, Cambridge CB2 1EZ, UK; fax: +44 1223 336033.

AUTHOR INFORMATION

Corresponding Authors

Arindam Mukherjee − *Department of Chemical Sciences and Centre for Advanced Functional Materials, Indian Institute of Science Education and Research (IISER) Kolkata, Mohanpur 741246, India*; orcid.org/0000-0001-9545-8628; Email: a.mukherjee@iiserkol.ac.in

Arnab Gupta − *Department of Biological Sciences, Indian Institute of Science Education and Research (IISER) Kolkata, Mohanpur 741246, India*; Email: arnab.gupta@iiserkol.ac.in

Authors

Rishav Chatterjee − *Department of Chemical Sciences, Indian Institute of Science Education and Research (IISER) Kolkata, Mohanpur 741246, India*

Indira Bhattacharya − *Department of Biological Sciences, Indian Institute of Science Education and Research (IISER) Kolkata, Mohanpur 741246, India*

Souryadip Roy − *Department of Chemical Sciences, Indian Institute of Science Education and Research (IISER) Kolkata, Mohanpur 741246, India*

Kallol Purkait − *Department of Chemical Sciences, Indian Institute of Science Education and Research (IISER) Kolkata, Mohanpur 741246, India*

Tuhin Subhra Koley − *Department of Chemical Sciences, Indian Institute of Science Education and Research (IISER) Kolkata, Mohanpur 741246, India*

Complete contact information is available at: https://pubs.acs.org/10.1021/acs.inorgchem.1c01363

Author Contributions

†Equal contributions.

Author Contributions

R.C. performed the synthesis, characterization, and in vitro (MTT) screening. I.B. performed immunofluorescence, immunoblot, and AO assay and contributed to the writing of the manuscript. S.R. performed 72 h stability tests for complex **4**, HEK293 antiproliferative activity, and Annexin-V assay. K.P. helped in the characterization and in vitro (MTT) screening. T.S.K. recorded the time-dependent NMR data for the 24 h stability studies. A.M. contributed to the design and supervision, while A.G. supervised most of the biological assays including immunofluorescence and Western blot studies.

Notes

The authors declare no competing financial interest.

ACKNOWLEDGMENTS

The authors earnestly acknowledge funding from CSIR, Government of India, via 01(2927)/2018/EMR-II and SERB via EMR/2017/002324 (for A.M.) for the microplate reader. They also thank IISER Kolkata for infrastructural and financial support. R.C. and S.R. thank INSPIRE, I.B. thanks CSIR, and T.S.K. thanks IISER Kolkata for providing research fellowships. R.C. thanks Dr. Sourav Acharya for antiproliferative activity data of oxaliplatin. A.G. is grateful for an Early Career Research Award from the Department of Science and Technology, Government of India (ECR/2015/000220) and a Wellcome Trust-DBT India Alliance Fellowship (IA/I/16/1/502369). We thank Tamal Ghosh for helping us with the flow cytometry analysis studies.

REFERENCES

(1) Kenny, R. G.; Marmion, C. J. Toward Multi-Targeted Platinum and Ruthenium Drugs-A New Paradigm in Cancer Drug Treatment Regimens? *Chem. Rev.* **2019**, *119* (2), 1058−1137.

(2) Florea, A.-M.; Buesselberg, D. Cisplatin as an anti-tumor drug: cellular mechanisms of activity, drug resistance and induced side effects. *Cancers* **2011**, *3*, 1351−1371.

(3) Dilruba, S.; Kalayda, G. V. Platinum-based drugs: past, present and future. *Cancer Chemother. Pharmacol.* **2016**, *77* (6), 1103−1124.

(4) Johnstone, T. C.; Suntharalingam, K.; Lippard, S. J. The Next Generation of Platinum Drugs: Targeted Pt(II) Agents, Nanoparticle Delivery, and Pt(IV) Prodrugs. *Chem. Rev.* **2016**, *116* (5), 3436−3486.

(5) Zhou, J.; Kang, Y.; Chen, L.; Wang, H.; Liu, J.; Zeng, S.; Yu, L. The Drug-Resistance Mechanisms of Five Platinum-Based Antitumor Agents. *Front. Pharmacol.* **2020**, *11*, 343.

(6) Oun, R.; Moussa, Y. E.; Wheate, N. J. The side effects of platinum-based chemotherapy drugs: a review for chemists. *Dalton Trans.* **2018**, *47* (19), 6645−6653.

(7) Hua, W.; Xu, G.; Zhao, J.; Wang, Z.; Lu, J.; Sun, W.; Gou, S. DNA-Targeting RuII-Polypyridyl Complex with a Long-Lived Intraligand Excited State as a Potential Photodynamic Therapy Agent. *Chem. - Eur. J.* **2020**, *26* (72), 17495−17503.

(8) Crlikova, H.; Kostrhunova, H.; Pracharova, J.; Kozsup, M.; Nagy, S.; Buglyó, P.; Brabec, V.; Kasparkova, J. Antiproliferative, DNA binding, and cleavage properties of dinuclear Co(III) complexes containing the bioactive quinizarin ligand. *JBIC, J. Biol. Inorg. Chem.* **2020**, *25* (2), 339−350.

(9) Mukherjee, A.; Acharya, S.; Purkait, K.; Chakraborty, K.; Bhattacharjee, A.; Mukherjee, A. Effect of N,N Coordination and RuII Halide Bond in Enhancing Selective Toxicity of a Tyramine-Based RuII (p-Cymene) Complex. *Inorg. Chem.* **2020**, *59* (9), 6581−6594.

(10) Maji, M.; Acharya, S.; Maji, S.; Purkait, K.; Gupta, A.; Mukherjee, A. Differences in Stability, Cytotoxicity, and Mechanism of Action of Ru(II) and Pt(II) Complexes of a Bidentate N,O Donor Ligand. *Inorg. Chem.* **2020**, *59* (14), 10262−10274.

(11) Purkait, K.; Ruturaj; Mukherjee, A.; Gupta, A. ATP7B Binds Ruthenium(II) p-Cymene Half-Sandwich Complexes: Role of Steric Hindrance and Ru−I Coordination in Rescuing the Sequestration. *Inorg. Chem.* **2019**, *58* (22), 15659−15670.

(12) Notaro, A.; Jakubaszek, M.; Rotthowe, N.; Maschietto, F.; Vinck, R.; Felder, P. S.; Goud, B.; Tharaud, M.; Ciofini, I.; Bedioui, F.; Winter, R. F.; Gasser, G. Increasing the Cytotoxicity of Ru(II) Polypyridyl Complexes by Tuning the Electronic Structure of Dioxo Ligands. *J. Am. Chem. Soc.* **2020**, *142* (13), 6066−6084.

(13) Maji, M.; Karmakar, S.; Ruturaj; Gupta, A.; Mukherjee, A. Oxamusplatin: a cytotoxic Pt(ii) complex of a nitrogen mustard with resistance to thiol based sequestration displays enhanced selectivity towards cancer. *Dalton Trans.* **2020**, *49* (8), 2547−2558.

(14) Leal, J.; Santos, L.; Fernández-Aroca, D. M.; Cuevas, J. V.; Martínez, M. A.; Massaguer, A.; Jalón, F. A.; Ruiz-Hidalgo, M. J.; Sánchez-Prieto, R.; Rodríguez, A. M.; Castañeda, G.; Durá, G.; Carrión, M. C.; Barrabés, S.; Manzano, B. R. Effect of the aniline fragment in Pt(II) and Pt(IV) complexes as anti-proliferative agents. Standard reduction potential as a more reliable parameter for Pt(IV) compounds than peak reduction potential. *J. Inorg. Biochem.* **2021**, *218*, 111403.

(15) Hummer, A. A.; Bartel, C.; Arion, V. B.; Jakupec, M. A.; Meyer-Klaucke, W.; Geraki, T.; Quinn, P. D.; Mijovilovich, A.; Keppler, B. K.; Rompel, A. X-ray Absorption Spectroscopy of an Investigational

https://doi.org/10.1021/acs.inorgchem.1c01363
Inorg. Chem. XXXX, XXX, XXX−XXX

Anticancer Gallium(III) Drug: Interaction with Serum Proteins, Elemental Distribution Pattern, and Coordination of the Compound in Tissue. *J. Med. Chem.* **2012**, *55* (11), 5601−5613.
(16) Enyedy, É. A.; Dömötör, O.; Varga, E.; Kiss, T.; Trondl, R.; Hartinger, C. G.; Keppler, B. K. Comparative solution equilibrium studies of anticancer gallium(III) complexes of 8-hydroxyquinoline and hydroxy(thio)pyrone ligands. *J. Inorg. Biochem.* **2012**, *117*, 189−197.
(17) Smithen, D. A.; Yin, H.; Beh, M. H. R.; Hetu, M.; Cameron, T. S.; McFarland, S. A.; Thompson, A. Synthesis and Photobiological Activity of Ru(II) Dyads Derived from Pyrrole-2-carboxylate Thionoesters. *Inorg. Chem.* **2017**, *56* (7), 4121−4132.
(18) Monro, S.; Colón, K. L.; Yin, H.; Roque, J.; Konda, P.; Gujar, S.; Thummel, R. P.; Lilge, L.; Cameron, C. G.; McFarland, S. A. Transition Metal Complexes and Photodynamic Therapy from a Tumor-Centered Approach: Challenges, Opportunities, and Highlights from the Development of TLD1433. *Chem. Rev.* **2019**, *119* (2), 797−828.
(19) Enyedy, É. A.; Dömötör, O.; Bali, K.; Hetényi, A.; Tuccinardi, T.; Keppler, B. K. Interaction of the anticancer gallium(III) complexes of 8-hydroxyquinoline and maltol with human serum proteins. *JBIC, J. Biol. Inorg. Chem.* **2015**, *20* (1), 77−88.
(20) Wernitznig, D.; Kiakos, K.; Del Favero, G.; Harrer, N.; Machat, H.; Osswald, A.; Jakupec, M. A.; Wernitznig, A.; Sommergruber, W.; Keppler, B. K. First-in-class ruthenium anticancer drug (KP1339/IT-139) induces an immunogenic cell death signature in colorectal spheroids in vitro†. *Metallomics* **2019**, *11* (6), 1044−1048.
(21) Neuditschko, B.; Legin, A. A.; Baier, D.; Schintlmeister, A.; Reipert, S.; Wagner, M.; Keppler, B. K.; Berger, W.; Meier-Menches, S. M.; Gerner, C. Interaction with Ribosomal Proteins Accompanies Stress Induction of the Anticancer Metallodrug BOLD-100/KP1339 in the Endoplasmic Reticulum. *Angew. Chem., Int. Ed.* **2021**, *60* (10), 5063−5068.
(22) Chitambar, C. R. Gallium Complexes as Anticancer Drugs. *Metal Ions Life Sci.* **2018**, *18*
(23) de Camargo, M. S.; De Grandis, R. A.; da Silva, M. M.; da Silva, P. B.; Santoni, M. M.; Eismann, C. E.; Menegário, A. A.; Cominetti, M. R.; Zanelli, C. F.; Pavan, F. R.; Batista, A. A. Determination of in vitro absorption in Caco-2 monolayers of anticancer Ru(II)-based complexes acting as dual human topoisomerase and PARP inhibitors. *BioMetals* **2019**, *32* (1), 89−100.
(24) Lenis-Rojas, O. A.; Robalo, M. P.; Tomaz, A. I.; Fernandes, A. R.; Roma-Rodrigues, C.; Teixeira, R. G.; Marques, F.; Folgueira, M.; Yáñez, J.; Gonzalez, A. A.; Salamini-Montemurri, M.; Pech-Puch, D.; Vázquez-García, D.; Torres, M. L.; Fernández, A.; Fernández, J. J. Half-Sandwich Ru(p-cymene) Compounds with Diphosphanes: In Vitro and In Vivo Evaluation As Potential Anticancer Metallodrugs. *Inorg. Chem.* **2021**, *60* (5), 2914−2930.
(25) Maji, M.; Acharya, S.; Bhattacharya, I.; Gupta, A.; Mukherjee, A. Effect of an Imidazole-Containing Schiff Base of an Aromatic Sulfonamide on the Cytotoxic Efficacy of N,N-Coordinated Half-Sandwich Ruthenium(II) p-Cymene Complexes. *Inorg. Chem.* **2021**, *60* (7), 4744−4754.
(26) Maji, M.; Bhattacharya, I.; Acharya, S.; Chakraborty, M. P.; Gupta, A.; Mukherjee, A. Hypoxia Active Platinum(IV) Prodrugs of Orotic Acid Selective to Liver Cancer Cells. *Inorg. Chem.* **2021**, *60* (7), 4342−4346.
(27) Acharya, S.; Maji, M.; Chakraborty, M. P.; Bhattacharya, I.; Das, R.; Gupta, A.; Mukherjee, A. Disruption of the Microtubule Network and Inhibition of VEGFR2 Phosphorylation by Cytotoxic N,O-Coordinated Pt(II) and Ru(II) Complexes of Trimethoxy Aniline-Based Schiff Bases. *Inorg. Chem.* **2021**, *60* (5), 3418−3430.
(28) Acharya, S.; Maji, M.; Ruturaj; Purkait, K.; Gupta, A.; Mukherjee, A. Synthesis, Structure, Stability, and Inhibition of Tubulin Polymerization by RuII−p-Cymene Complexes of Trimethoxyaniline-Based Schiff Bases. *Inorg. Chem.* **2019**, *58* (14), 9213−9224.
(29) Ilmi, R.; Tseriotou, E.; Stylianou, P.; Christou, Y. A.; Ttofi, I.; Dietis, N.; Pitris, C.; Odysseos, A. D.; Georgiades, S. N. A Novel Conjugate of Bis[((4-bromophenyl)amino)quinazoline], a EGFR-TK Ligand, with a Fluorescent Ru(II)-Bipyridine Complex Exhibits Specific Subcellular Localization in Mitochondria. *Mol. Pharmaceutics* **2019**, *16* (10), 4260−4273.
(30) Sonkar, C.; Malviya, N.; Ranjan, R.; Pakhira, S.; Mukhopadhyay, S. Mechanistic Insight for Targeting Biomolecules by Ruthenium(II) NSAID Complexes. *ACS Appl. Bio Mater.* **2020**, *3* (7), 4600−4612.
(31) Mondal, A.; Sen, U.; Roy, N.; Muthukumar, V.; Sahoo, S. K.; Bose, B.; Paira, P. DNA targeting half sandwich Ru(ii)-p-cymene-N∧N complexes as cancer cell imaging and terminating agents: influence of regioisomers in cytotoxicity. *Dalton Trans.* **2021**, *50* (3), 979−997.
(32) Qiao, L.; Liu, J.; Han, Y.; Wei, F.; Liao, X.; Zhang, C.; Xie, L.; Ji, L.; Chao, H. Rational design of a lysosome-targeting and near-infrared absorbing Ru(ii)−BODIPY conjugate for photodynamic therapy. *Chem. Commun.* **2021**, *57* (14), 1790−1793.
(33) Zhang, C.; Guan, R.; Liao, X.; Ouyang, C.; Rees, T. W.; Liu, J.; Chen, Y.; Ji, L.; Chao, H. A mitochondria-targeting dinuclear Ir−Ru complex as a synergistic photoactivated chemotherapy and photodynamic therapy agent against cisplatin-resistant tumour cells. *Chem. Commun.* **2019**, *55* (83), 12547−12550.
(34) Acharya, S.; Ghosh, S.; Maji, M.; Parambil, A. R. U.; Singh, S.; Mukherjee, A. Inhibition of 3D colon cancer stem cell spheroids by cytotoxic RuII-p-cymene complexes of mesalazine derivatives. *Chem. Commun.* **2020**, *56* (40), 5421−5424.
(35) Liu, R.; Yuan, C.; Feng, Y.; Qian, J.; Huang, X.; Chen, Q.; Zhou, S.; Ding, Y.; Zhai, B.; Mei, W.; Yao, L. Microwave-assisted synthesis of ruthenium(ii) complexes containing levofloxacin-induced G2/M phase arrest by triggering DNA damage. *RSC Adv.* **2021**, *11* (8), 4444−4453.
(36) Steel, T. R.; Walsh, F.; Wieczorek-Błauż, A.; Hanif, M.; Hartinger, C. G. Monodentately-coordinated bioactive moieties in multimodal half-sandwich organoruthenium anticancer agents. *Coord. Chem. Rev.* **2021**, *439*, 213890.
(37) Liu, Z.; Li, J.; Kong, D.; Tian, M.; Zhao, Y.; Xu, Z.; Gao, W.; Zhou, Y. Dual Functional Half-Sandwich Ru(II) Complexes: Lysosome-Targeting Probes and Anticancer Agents. *Eur. J. Inorg. Chem.* **2019**, *2019* (2), 287−294.
(38) Hartinger, C. G.; Zorbas-Seifried, S.; Jakupec, M. A.; Kynast, B.; Zorbas, H.; Keppler, B. K. From bench to bedside − preclinical and early clinical development of the anticancer agent indazolium trans-[tetrachlorobis(1H-indazole)ruthenate(III)] (KP1019 or FFC14A). *J. Inorg. Biochem.* **2006**, *100* (5), 891−904.
(39) Motswainyana, W. M.; Ajibade, P. A. Anticancer activities of mononuclear ruthenium (II) coordination complexes. *Adv. Chem.* **2015**, *2015*, 1.
(40) Lin, K.; Zhao, Z.-Z.; Bo, H.-B.; Hao, X.-J.; Wang, J.-Q. Applications of ruthenium complex in tumor diagnosis and therapy. *Front. Pharmacol.* **2018**, *9*, 1323.
(41) Kostova, I. Ruthenium complexes as anticancer agents. *Curr. Med. Chem.* **2006**, *13* (9), 1085−1107.
(42) Wang, Y.; Jin, J.; Shu, L.; Li, T.; Lu, S.; Subarkhan, M. K. M.; Chen, C.; Wang, H. New Organometallic Ruthenium(II) Compounds Synergistically Show Cytotoxic, Antimetastatic and Antiangiogenic Activities for the Treatment of Metastatic Cancer. *Chem. - Eur. J.* **2020**, *26* (66), 15170−15182.
(43) Travassos, I. O.; Mello-Andrade, F.; Caldeira, R. P.; Pires, W. C.; da Silva, P. F. F.; Correa, R. S.; Teixeira, T.; Martins-Oliveira, A.; Batista, A. A.; de Silveira-Lacerda, E. P. Ruthenium (II)/allopurinol complex inhibits breast cancer progression via multiple targets. *JBIC, J. Biol. Inorg. Chem.* **2021**, *26*, 385.
(44) Ribeiro, G. H.; Guedes, A. P. M.; de Oliveira, T. D.; de Correia, C. R. S. T. b.; Colina-Vegas, L.; Lima, M. A.; Nóbrega, J. A.; Cominetti, M. R.; Rocha, F. V.; Ferreira, A. G.; Castellano, E. E.; Teixeira, F. R.; Batista, A. A. Ruthenium(II) Phosphine/Mercapto Complexes: Their in Vitro Cytotoxicity Evaluation and Actions as Inhibitors of Topoisomerase and Proteasome Acting as Possible

https://doi.org/10.1021/acs.inorgchem.1c01363
Inorg. Chem. XXXX, XXX, XXX−XXX

Triggers of Cell Death Induction. *Inorg. Chem.* **2020**, *59* (20), 15004−15018.
(45) Karmakar, J.; Nandy, P.; Das, S.; Bhattacharya, D.; Karmakar, P.; Bhattacharya, S. Utilization of Guanidine-Based Ancillary Ligands in Arene−Ruthenium Complexes for Selective Cytotoxicity. *ACS Omega* **2021**, *6* (12), 8226−8238.
(46) Jin, Z.; Qi, S.; Guo, X.; Jian, Y.; Hou, Y.; Li, C.; Wang, X.; Zhou, Q. The modification of a pyrene group makes a Ru(ii) complex versatile. *Chem. Commun.* **2021**, *57* (26), 3259−3262.
(47) Wise, D. E.; Gamble, A. J.; Arkawazi, S. W.; Walton, P. H.; Galan, M. C.; O'Hagan, M. P.; Hogg, K. G.; Marrison, J. L.; O'Toole, P. J.; Sparkes, H. A.; Lynam, J. M.; Pringle, P. G. Cytotoxic (cis,cis-1,3,5-triaminocyclohexane)ruthenium(ii)-diphosphine complexes; evidence for covalent binding and intercalation with DNA. *Dalton Trans.* **2020**, *49* (43), 15219−15230.
(48) Pereira, S. A. P.; Bobbink, F. D.; Dyson, P. J.; Saraiva, M. L. M. F. S. Automatic evaluation of cyclooxygenase 2 inhibition induced by metal-based anticancer compounds. *J. Inorg. Biochem.* **2021**, *218*, 111399.
(49) Du, E.; Hu, X.; Roy, S.; Wang, P.; Deasy, K.; Mochizuki, T.; Zhang, Y. Taurine-modified Ru (II)-complex targets cancerous brain cells for photodynamic therapy. *Chem. Commun.* **2017**, *53* (44), 6033−6036.
(50) Du, Q.; Guo, L.; Ge, X.; Zhao, L.; Tian, Z.; Liu, X.; Zhang, F.; Liu, Z. Serendipitous synthesis of five-coordinated half-sandwich aminoimine iridium (iii) and ruthenium (ii) complexes and their application as potent anticancer agents. *Inorg. Chem.* **2019**, *58* (9), 5956−5965.
(51) Li, J.; Tian, Z.; Ge, X.; Xu, Z.; Feng, Y.; Liu, Z. Design, synthesis, and evaluation of fluorine and Naphthyridine−Based half-sandwich organoiridium/ruthenium complexes with bioimaging and anticancer activity. *Eur. J. Med. Chem.* **2019**, *163*, 830−839.
(52) Li, J.; Tian, Z.; Xu, Z.; Zhang, S.; Feng, Y.; Zhang, L.; Liu, Z. Highly potent half-sandwich iridium and ruthenium complexes as lysosome-targeted imaging and anticancer agents. *Dalton Trans.* **2018**, *47* (44), 15772−15782.
(53) Ma, W.; Guo, L.; Tian, Z.; Zhang, S.; He, X.; Li, J.; Yang, Y.; Liu, Z. Rhodamine-modified fluorescent half-sandwich iridium and ruthenium complexes: potential application as bioimaging and anticancer agents. *Dalton Trans.* **2019**, *48* (15), 4788−4793.
(54) Ma, W.; Zhang, S.; Tian, Z.; Xu, Z.; Zhang, Y.; Xia, X.; Chen, X.; Liu, Z. Potential anticancer agent for selective damage to mitochondria or lysosomes: Naphthalimide-modified fluorescent biomarker half-sandwich iridium (III) and ruthenium (II) complexes. *Eur. J. Med. Chem.* **2019**, *181*, 111599.
(55) Mitrović, A.; Kljun, J.; Sosič, I.; Gobec, S.; Turel, I.; Kos, J. Clioquinol−ruthenium complex impairs tumour cell invasion by inhibiting cathepsin B activity. *Dalton Trans.* **2016**, *45* (42), 16913−16921.
(56) Mitrović, A.; Kljun, J.; Sosič, I.; Uršič, M.; Meden, A.; Gobec, S.; Kos, J.; Turel, I. Organoruthenated nitroxoline derivatives impair tumor cell invasion through inhibition of cathepsin B activity. *Inorg. Chem.* **2019**, *58* (18), 12334−12347.
(57) Paitandi, R. P.; Sharma, V.; Singh, V. D.; Dwivedi, B. K.; Mobin, S. M.; Pandey, D. S. Pyrazole appended quinoline-BODIPY based arene ruthenium complexes: their anticancer activity and potential applications in cellular imaging. *Dalton Trans.* **2018**, *47* (48), 17500−17514.
(58) Thota, S.; Rodrigues, D. A.; Crans, D. C.; Barreiro, E. J. Ru (II) compounds: next-generation anticancer metallotherapeutics? *J. Med. Chem.* **2018**, *61* (14), 5805−5821.
(59) Xie, Y.; Zhang, S.; Ge, X.; Ma, W.; He, X.; Zhao, Y.; Ye, J.; Zhang, H.; Wang, A.; Liu, Z. Lysosomal-targeted anticancer half-sandwich iridium (III) complexes modified with lonidamine amide derivatives. *Appl. Organomet. Chem.* **2020**, *34* (5), e5589.
(60) Yang, Y.; Guo, L.; Tian, Z.; Gong, Y.; Zheng, H.; Zhang, S.; Xu, Z.; Ge, X.; Liu, Z. Novel and versatile imine-N-heterocyclic carbene half-sandwich iridium (III) complexes as lysosome-targeted anticancer agents. *Inorg. Chem.* **2018**, *57* (17), 11087−11098.
(61) Yang, Y.; Guo, L.; Tian, Z.; Liu, X.; Gong, Y.; Zheng, H.; Ge, X.; Liu, Z. Imine-N-Heterocyclic Carbenes as Versatile Ligands in Ruthenium (II) p-Cymene Anticancer Complexes: A Structure−Activity Relationship Study. *Chem. - Asian J.* **2018**, *13* (19), 2923−2933.
(62) Zeng, L.; Gupta, P.; Chen, Y.; Wang, E.; Ji, L.; Chao, H.; Chen, Z.-S. The development of anticancer ruthenium (II) complexes: from single molecule compounds to nanomaterials. *Chem. Soc. Rev.* **2017**, *46* (19), 5771−5804.
(63) Kumari, A.; Singh, R. K. Morpholine as ubiquitous pharmacophore in medicinal chemistry: deep insight into the structure-activity relationship (SAR). *Bioorg. Chem.* **2020**, *96*, 103578.
(64) Kourounakis, A. P.; Xanthopoulos, D.; Tzara, A. Morpholine as a privileged structure: a review on the medicinal chemistry and pharmacological activity of morpholine containing bioactive molecules. *Med. Res. Rev.* **2020**, *40* (2), 709−752.
(65) Tzara, A.; Xanthopoulos, D.; Kourounakis, A. P. Morpholine As a Scaffold in Medicinal Chemistry: An Update on Synthetic Strategies. *ChemMedChem* **2020**, *15*, 392.
(66) Walker, E. H.; Pacold, M. E.; Perisic, O.; Stephens, L.; Hawkins, P. T.; Wymann, M. P.; Williams, R. L. Structural determinants of phosphoinositide 3-kinase inhibition by wortmannin, LY294002, quercetin, myricetin, and staurosporine. *Mol. Cell* **2000**, *6* (4), 909−919.
(67) Knight, Z. A.; Chiang, G. G.; Alaimo, P. J.; Kenski, D. M.; Ho, C. B.; Coan, K.; Abraham, R. T.; Shokat, K. M. Isoform-specific phosphoinositide 3-kinase inhibitors from an arylmorpholine scaffold. *Bioorg. Med. Chem.* **2004**, *12* (17), 4749−4759.
(68) Vlahos, C. J.; Matter, W. F.; Hui, K. Y.; Brown, R. F. A specific inhibitor of phosphatidylinositol 3-kinase, 2-(4-morpholinyl)-8-phenyl-4H-1-benzopyran-4-one (LY294002). *J. Biol. Chem.* **1994**, *269* (7), 5241−5248.
(69) Zask, A.; Kaplan, J.; Verheijen, J. C.; Richard, D. J.; Curran, K.; Brooijmans, N.; Bennett, E. M.; Toral-Barza, L.; Hollander, I.; Ayral-Kaloustian, S.; Yu, K. Morpholine derivatives greatly enhance the selectivity of mammalian target of rapamycin (mTOR) inhibitors. *J. Med. Chem.* **2009**, *52* (24), 7942−7945.
(70) Chresta, C. M.; Davies, B. R.; Hickson, I.; Harding, T.; Cosulich, S.; Critchlow, S. E.; Vincent, J. P.; Ellston, R.; Jones, D.; Sini, P.; et al. AZD8055 is a potent, selective, and orally bioavailable ATP-competitive mammalian target of rapamycin kinase inhibitor with in vitro and in vivo antitumor activity. *Cancer Res.* **2010**, *70* (1), 288−298.
(71) Zheng, J.; Xin, Y.; Zhang, J.; Subramanian, R.; Murray, B. P.; Whitney, J. A.; Warr, M. R.; Ling, J.; Moorehead, L.; Kwan, E.; Hemenway, J.; Smith, B. J.; Silverman, J. A. Pharmacokinetics and Disposition of Momelotinib Revealed a Disproportionate Human Metabolite—Resolution for Clinical Development. *Drug Metab. Dispos.* **2018**, *46* (3), 237−247.
(72) Liu, D.; Xu, Y.; Feng, Y.; Liu, H.; Shen, X.; Chen, K.; Ma, J.; Jiang, H. Inhibitor discovery targeting the intermediate structure of β-amyloid peptide on the conformational transition pathway: implications in the aggregation mechanism of β-amyloid peptide. *Biochemistry* **2006**, *45* (36), 10963−10972.
(73) Yun, C.-H.; Boggon, T. J.; Li, Y.; Woo, M. S.; Greulich, H.; Meyerson, M.; Eck, M. J. Structures of lung cancer-derived EGFR mutants and inhibitor complexes: mechanism of activation and insights into differential inhibitor sensitivity. *Cancer Cell* **2007**, *11* (3), 217−227.
(74) Barker, A. J.; Gibson, K. H.; Grundy, W.; Godfrey, A. A.; Barlow, J. J.; Healy, M. P.; Woodburn, J. R.; Ashton, S. E.; Curry, B. J.; Scarlett, L.; Henthorn, L.; Richards, L. Studies leading to the identification of ZD1839 (Iressa): an orally active, selective epidermal growth factor receptor tyrosine kinase inhibitor targeted to the treatment of cancer. *Bioorg. Med. Chem. Lett.* **2001**, *11* (14), 1911−1914.
(75) Falcone, S.; Cocucci, E.; Podini, P.; Kirchhausen, T.; Clementi, E.; Meldolesi, J. Macropinocytosis: regulated coordination of

https://doi.org/10.1021/acs.inorgchem.1c01363
Inorg. Chem. XXXX, XXX, XXX−XXX

endocytic and exocytic membrane traffic events. *J. Cell Sci.* **2006**, *119* (22), 4758−4769.
(76) Alberts, B.; Johnson, A.; Lewis, J.; Raff, M.; Roberts, K.; Walter, P. *Molecular Biology of the Cell*, 4th ed.; Garland Science, 2002.
(77) Armarego, W. L. F.; Chai, C. In *Purification of Laboratory Chemicals*, 7th ed.; Armarego, W. L. F., Chai, C., Eds.; Butterworth-Heinemann: Boston, 2013; pp 71−90.
(78) Sashuk, V.; Schoeps, D.; Plenio, H. Fluorophore tagged cross-coupling catalysts. *Chem. Commun.* **2009**, *7*, 770−772.
(79) Oliveira, K. M.; Honorato, J.; Gonçalves, G. R.; Cominetti, M. R.; Batista, A. A.; Correa, R. S. Ru(ii)/diclofenac-based complexes: DNA, BSA interaction and their anticancer evaluation against lung and breast tumor cells. *Dalton Trans.* **2020**, *49* (36), 12643−12652.
(80) OECD. *Test No. 107: Partition Coefficient (n-octanol/water): Shake Flask Method*, 1995.
(81) Purkait, K.; Chatterjee, S.; Karmakar, S.; Mukherjee, A. Alteration of steric hindrance modulates glutathione resistance and cytotoxicity of three structurally related Ru^{II}-p-cymene complexes. *Dalton Trans.* **2016**, *45* (20), 8541−8555.
(82) Bhattacharyya, S.; Purkait, K.; Mukherjee, A. Ruthenium(II) p-cymene complexes of a benzimidazole-based ligand capable of VEGFR2 inhibition: hydrolysis, reactivity and cytotoxicity studies. *Dalton Trans.* **2017**, *46* (26), 8539−8554.
(83) Ramos, T. S.; Luz, D. M.; Nascimento, R. D.; Silva, A. K.; Lião, L. M.; Miranda, V. M.; Deflon, V. M.; de Araujo, M. P.; Ueno, L. T.; Machado, F. B. C.; Dinelli, L. R.; Bogado, A. L. Ruthenium-cymene containing pyridine-derived aldiimine ligands: Synthesis, characterization and application in the transfer hydrogenation of aryl ketones and kinetics studies. *J. Organomet. Chem.* **2019**, *892*, 51−65.
(84) Wenlock, M. C.; Potter, T.; Barton, P.; Austin, R. P. A method for measuring the lipophilicity of compounds in mixtures of 10. *J. Biomol. Screening* **2011**, *16* (3), 348−355.
(85) Chen, J. W.; Murphy, T. L.; Willingham, M. C.; Pastan, I.; August, J. T. Identification of two lysosomal membrane glycoproteins. *J. Cell Biol.* **1985**, *101* (1), 85−95.
(86) Kundra, R.; Kornfeld, S. Asparagine-linked oligosaccharides protect Lamp-1 and Lamp-2 from intracellular proteolysis. *J. Biol. Chem.* **1999**, *274* (43), 31039−31046.
(87) Boya, P.; Kroemer, G. Lysosomal membrane permeabilization in cell death. *Oncogene* **2008**, *27* (50), 6434−6451.
(88) Xiao, L.; Wang, Y. C.; Li, W. S.; Du, Y. The role of mTOR and phospho-p70S6K in pathogenesis and progression of gastric carcinomas: an immunohistochemical study on tissue microarray. *J. Exp. Clin. Cancer Res.* **2009**, *28* (1), 152.
(89) Liu, H.; Huang, B.; Xue, S.; U, K. P.; Tsang, L. L.; Zhang, X.; Li, G.; Jiang, X. Functional crosstalk between mTORC1/p70S6K pathway and heterochromatin organization in stress-induced senescence of MSCs. *Stem Cell Res. Ther.* **2020**, *11* (1), 279.
(90) Satyavarapu, E. M.; Das, R.; Mandal, C.; Mukhopadhyay, A.; Mandal, C. Autophagy-independent induction of LC3B through oxidative stress reveals its non-canonical role in anoikis of ovarian cancer cells. *Cell Death Dis.* **2018**, *9* (10), 934.
(91) Wu, J.; Dang, Y.; Su, W.; Liu, C.; Ma, H.; Shan, Y.; Pei, Y.; Wan, B.; Guo, J.; Yu, L. Molecular cloning and characterization of rat LC3A and LC3B—Two novel markers of autophagosome. *Biochem. Biophys. Res. Commun.* **2006**, *339* (1), 437−442.
(92) Tanida, I.; Ueno, T.; Kominami, E. Human Light Chain 3/MAP1LC3B Is Cleaved at Its Carboxyl-terminal Met121 to Expose Gly120 for Lipidation and Targeting to Autophagosomal Membranes*. *J. Biol. Chem.* **2004**, *279* (46), 47704−47710.
(93) Kabeya, Y.; Mizushima, N.; Yamamoto, A.; Oshitani-Okamoto, S.; Ohsumi, Y.; Yoshimori, T. LC3, GABARAP and GATE16 localize to autophagosomal membrane depending on form-II formation. *J. Cell Sci.* **2004**, *117*, 2805−2812.
(94) Kabeya, Y. LC3, a mammalian homolog of yeast Apg8p, is localized in autophagosome membranes after processing. *EMBO J.* **2000**, *19* (21), 5720.
(95) He, H.; Dang, Y.; Dai, F.; Guo, Z.; Wu, J.; She, X.; Pei, Y.; Chen, Y.; Ling, W.; Wu, C.; Zhao, S.; Liu, J. O.; Yu, L. Post-translational Modifications of Three Members of the Human MAP1LC3 Family and Detection of a Novel Type of Modification for MAP1LC3B*. *J. Biol. Chem.* **2003**, *278* (31), 29278−29287.
(96) Ichimura, Y.; Kirisako, T.; Takao, T.; Satomi, Y.; Shimonishi, Y.; Ishihara, N.; Mizushima, N.; Tanida, I.; Kominami, E.; Ohsumi, M.; Noda, T.; Ohsumi, Y. A ubiquitin-like system mediates protein lipidation. *Nature* **2000**, *408* (6811), 488−492.
(97) Cleary, M. L.; Smith, S. D.; Sklar, J. Cloning and structural analysis of cDNAs for bcl-2 and a hybrid bcl-2/immunoglobulin transcript resulting from the t(14;18) translocation. *Cell* **1986**, *47* (1), 19−28.
(98) Tsujimoto, Y.; Finger, L.; Yunis, J.; Nowell, P.; Croce, C. Cloning of the chromosome breakpoint of neoplastic B cells with the t(14;18) chromosome translocation. *Science* **1984**, *226* (4678), 1097−1099.
(99) Kelly, G. L.; Strasser, A. Toward Targeting Antiapoptotic MCL-1 for Cancer Therapy. *Annu. Rev. Cancer Biol.* **2020**, *4* (1), 299−313.

https://doi.org/10.1021/acs.inorgchem.1c01363
Inorg. Chem. XXXX, XXX, XXX−XXX